Identification of potential antifibrinolytic compounds against kringle-1 and serine protease domain of plasminogen and kringle-2 domain of tissue-type plasminogen activator using combined virtual screening, molecular docking, and molecular dynamics simulation approaches

Running Title: Identification of potential antifibrinolytic compounds against plasminogen and tissue-type plasminogen activator

Suparna Banerjee*[1], Yeshwanth. M*[2], D. Prabhu[3], K. Sekar [2] and Prosenjit Sen[#1]

[1]School of Biological Sciences, Indian Association for the Cultivation of Science, Jadavpur, Kolkata 700032, West Bengal, India

[2] Department of Computational and Data Sciences, Indian Institute of Science, Bangalore 560012, Karnataka, India

[3]Research and Development Wing, Sree Balaji Medical College and Hospital, Chrompet, Chennai 600044, Tamil Nadu, India

* These authors have made equal contribution, and should be treated as co-first authors

[#]Author to whom correspondence should be addressed: bcps@iacs.res.in (Prosenjit Sen)

Graphical Abstract

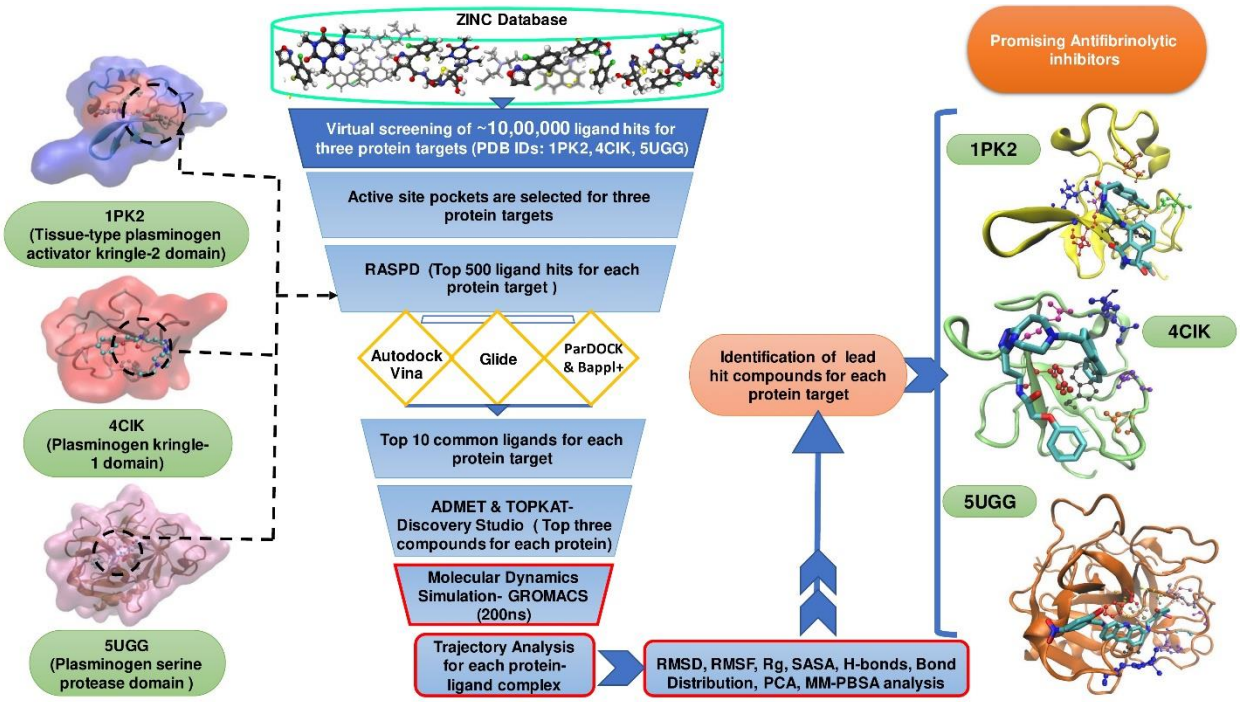

Abstract

Background: The zymogen protease Plasminogen (Plg) and its active form plasmin (Plm) carry out important functions in the blood clot disintegration (breakdown of fibrin fibres) process. Inhibition of plasmin effectively reduces fibrinolysis to circumvent heavy bleeding. Currently, available Plm inhibitor tranexamic acid (TXA) that is used to treat severe hemorrhages is associated with an increased incidence of seizures which in turn were traced to gamma-aminobutyric acid (GABA) antagonistic activity in addition to having multiple side effects.

Methods: Fibrinolysis can be suppressed by targeting the three important protein domains: kringle-1 and serine protease domain of plasminogen and kringle-2 domain of tissue plasminogen activator. In the present study, combined approaches of structure-based virtual screening and molecular docking using Schrodinger-Glide, Autodock-Vina, and ParDOCK/BAPPL+ were employed to identify potential hits from the ZINC database. Thereafter, the drug-likeness properties of the top three leads were evaluated using Discovery Studio. Subsequently, molecular dynamics simulation of 200ns for each protein-ligand complex was performed in GROMACS.

Results: The identified ligands are found to impart higher rigidity and stability to the protein-ligand complexes. Furthermore, the results were validated by performing the principal component analysis (PCA), and binding free energy was calculated using the Molecular Mechanics Poisson-Boltzmann Surface Area (MMPBSA) approach.

Conclusion: The identified ligands occupy smaller phase space, form stable clusters and exhibit stronger non-bonded interactions. Thus, our findings can be useful for the development of promising anti-fibrinolytic agents.

Keywords: plasmin; structure-based virtual screening; molecular docking; molecular dynamics simulation; principal component analysis (PCA); Molecular Mechanics Poisson-Boltzmann Surface Area (MMPBSA)

Highlights

- Fibrinolysis can be inhibited by targeting the kringle-1 and serine protease domain of plasminogen and the kringle-2 domain of tissue plasminogen activator.
- Structure-based virtual screening and molecular docking approaches were employed to identify lead compounds from the ZINC database using Schrodinger-glide, Autodock-Vina, and ParDOCK/BAPPL+.
- The top three ligands were identified against each target followed by MD simulation, ADMET, PCA, and MMPBSA analysis.
- The identified ligands impart higher rigidity and stability to the protein-ligand complexes, exhibit stronger non-bonded interactions, and can help develop potent anti-fibrinolytic agents.

1. Introduction

Fibrinolysis is a process of removal (lysing) of clots formed due to the triggering of the hemostatic pathway, in conditions such as pathological thrombosis and vascular occlusion [1]. The principal mediator of fibrinolysis is plasminogen, which is transformed into plasmin by the plasminogen activators (Tissue-type plasminogen activator and Urokinase plasminogen activator) [2]. Tissue-type plasminogen activator (tPA or PLAT) is a serine protease found on the surface of endothelial cells that plays an important role in degrading polymerized fibrin by hydrolyzing the Arg560-Va1561 peptide bond in plasminogen (Plg) [3]. t-PA consists of six well-defined structural modules: a finger domain; an epidermal growth factor domain; two kringle domains and a serine protease two-domain unit with trypsin-like specificity [4]. Because of the presence of a lysine binding site in the above-mentioned two kringle domains and its stimulatory effect on Plg activation by fibrin, the scientific community has shown significant interest in the kringle domain [5]. The zymogen protease Plg and its active form plasmin (Plm), carry out important functions in blood clot disintegration apart from other cellular processes such as bacterial pathogenesis, tissue remodeling, and cell migration [6]. Plg comprises a serine protease (SP) domain, a Pan-apple (PAp) domain, and 5 kringle (KR 1-5) domains. These domains are ordered in a closed configuration that is sustained through interdomain interactions facilitated by the canonical lysine-binding sites (LBSs) of the KR domains. The binding of Plg to lysine-containing substrates or receptors is also facilitated by the LBSs of the KRs. Post binding, Plg takes an open configuration that is triggered by tissue plasminogen activators (tPAs) or urokinase plasminogen activators (uPAs) [7]. To regulate this binding process, α_2-antiplasmin and α_2-macroglobulin block the release of activated Plm from the clot or the cell surface [8]. Irregular balance of Plg/Plm system and immoderate fibrinolytic activity leads to fatal hemorrhagic disorders, thrombotic vascular injury, and severe complications during general surgery or major trauma [9]. Presently, the Plm inhibitors aprotinin and tranexamic acid (TXA) are clinically used to treat severe hemorrhages by blocking new entry to target substrates and are the most extensively used inhibitor for the Plg/Plm system [10]. TXA is a reasonably well-tolerated lysine analog that binds to the LBSs, culminating in the development of open Plg [11]. Post binding, TXA obstructs Plm activation by stopping it from binding to substrates and/or receptors. However, one recent study has shown that TXA may not block the activity of Plm which has already been formed leading to dangerous complications in patients suffering from extreme blood loss [12]. Hence, there is a requirement to synthesize

specific inhibitors which can attach to the protease active site of Plg. Cross reaction of Plm inhibitors with other plasma serine proteases also challenges their development because the reactions generate multiple side effects like headaches, nasal symptoms, or back, abdominal, and muscle pain. In some cases of treatment with TXA, seizures were reported as a side effect which in turn were traced to gamma-aminobutyric acid antagonistic activity (GABAa) [13]. Also, the gastrointestinal side effects associated with a high dose of TXA can be attributed to GABAa [14]**.** Based on the findings of these studies, the ideal novel oral fibrinolysis inhibitor is expected to work on a mechanism of action similar to that of TXA, having suitable dosing and higher selectivity over GABAa. Of late, some new encouraging drugs have been discovered like 4-PIOL and PS-112 (TXA-derived active site inhibitors) but, to date, their detailed profiling and testing have not been performed [15-16]. Even though considerable research has been undertaken, clinically safe fibrinolysis inhibitors have not reached the market. Fibrinolysis can be suppressed by targeting each of the three important protein domains: the kringle-2 domain of tissue plasminogen activator, the kringle-1 domain of plasminogen, and the serine protease domain of plasminogen. Previous studies reported that the catalytically active domain is constituted by the serine protease domain while the kringle domains are crucial for protein-protein interactions such as binding to fibrin [17]. Therefore, we have selected the above-mentioned three individual protein domains as our respective targets [18-20]. Herein, we attempt to find potential inhibitors having minimum side effects with maximum specificity and efficacy using *in silico* approaches. In this present study, combined approaches of structure-based virtual screening and molecular docking were employed to discern prospective hits from the ligand database [21]. Thereafter, ADMET (Absorption, Distribution, Metabolism, Excretion, and Toxicity) properties of these identified ligands were evaluated and a molecular dynamics simulation of 200ns was carried out for each protein-ligand complex. Furthermore, principal component analysis (PCA) was performed and binding free energy was calculated using the Molecular Mechanics Poisson-Boltzmann Surface Area (MMPBSA) approach for all the protein-ligand complexes. The identified lead compounds are expected to contribute to the development of potent anti-fibrinolytic agents.

2. Methods

2.1. Protein Preparation:

The crystal structures of the kringle-2 domain of tissue plasminogen activator, the kringle-1 domain of plasminogen, and the serine protease domain of plasminogen with PDB IDs: 1PK2, 4CIK, 5UGG were retrieved from the protein data bank (PDB) respectively [22-25]. All the three protein structures were analyzed in the pymol and discovery Studio 3.5 package (Accelrys, San Diego, CA, USA), and the missing residues in the structures were added using Modeller [26-28]. The co-crystallized ligands with IDs: ACA, XO3, 89M were extracted from protein crystal structures 1PK2, 4CIK, and 5UGG respectively using discovery Studio 3.5. The water molecules were eliminated, and protein preparation was done using the default settings of discovery Studio 3.5. Further, the protein structures were optimized using CHARMM (Chemistry at Harvard Macromolecular Mechanics) force field, and energy minimization was done by a smart minimizer algorithm incorporating conjugate gradient energy protocol [29]. Subsequently, these protein structures were selected as targets for virtual screening.

2.2. Structure-based virtual screening

The library of one million ligands was retrieved from the ZINC 15 database [30]**.** Initially, these one million ligands were screened individually against 1PK2, 4CIK, and 5UGG protein targets respectively using RASPD [31]. This tool rapidly identifies hit molecules against the protein targets based on their physicochemical properties and calculates the binding energy. Subsequently, the hits were further evaluated based on Lipinski parameters such as hydrogen bond acceptors & donors, molar refractivity, ADMET, Wiener index, and volume of functional groups & protein. The residues which were bound to the co-crystallized ligands were selected as active site pockets of the target proteins for virtual screening. From RASPD, the top 1500 hits (500 for each protein target) were retrieved for further analysis.

2.3 Molecular Docking

The top 500 hits filtered out from virtual screening (1500 total) were subjected to molecular docking against the three protein targets 1PK2, 4CIK, and 5UGG using three docking tools such as Autodock Vina**,** Glide**,** and ParDOCK/BAPPL+ respectively [32-35].

2.3.1. Glide (Grid-based ligand docking with energetic)

Firstly, the ligands were prepared using the LigPrep module of Schrodinger Maestro version 2.9, 2019 so that the ligands could be supplied to glide for docking in a state as they would occur in a protein-ligand complex [36]. LigPrep uses Optimized Potential Liquid Simulation (OPLS) 2005 force field and consists of a series of steps to optimize the structures. By default, LigPrep adds hydrogens, removes unwanted molecules, and minimizes the ligand structure. Thereafter, docking was performed using the software package Glide version 2.9, 2019. Protein structures were prepared in the Protein Preparation Wizard of Schrodinger in which proteins were refined by adding missing hydrogens and assigning proper bond orders. A grid file was generated using the Receptor Grid Generation protocol on these minimized structures, such that the grid points were adjusted to the active site pocket in X, Y, and Z dimensions with 25 × 25 × 25 points, and the ligands were allowed to move freely. We have used Glide docking modules namely simple precision (SP) and extra precision (XP) for docking calculations [37]. The conformations obtained from SP were used as input for XP to generate multiple binding poses. The binding affinity was computed based on the glide scoring function for all the three target proteins i.e., 1PK2, 4CIK, and 5UGG respectively. Thereafter, the top ten ligands were ranked according to their binding affinity using GScore (GlideScore) scoring function which is a combination of Coulombic energies, Van der Waals energies, and the internal strain of the ligand [38].

GScore = 0.065*vdW + 0.130*Coul + Lipo + Hbond + Metal + BuryP + RotB + Site. where,

Glide evdW - Van der Waal energy

Glide Ecoul - Coulomb energy

Glide Lipo - Lipophilic contact term

Glide Hbond - Hydrogen-bonding term

Glide Metal- Metal-binding term

Glide BuryP- Penalty for buried polar groups

Glide RotB- Penalty for freezing rotatable bonds

Glide Site- Polar interactions in the active site

2.3.2. Auto Dock Vina

As mentioned earlier, 1500 hits (500 hits per protein) were processed and subjected to docking analysis in AutoDock Vina. ADT tool was used to load the target protein structure and convert proteins to PDBQT format. Subsequently, the ligand hits were also converted into PDBQT format in Open Babel [39]. The hydrogen atoms and water molecules from the protein structure were removed and polar hydrogen atoms were added. Thereafter, Kollman charges were incorporated into the target protein structures [40]. The auto-grid box was set across X-Y-Z directions, i.e., 23x20x18 points for tissue-type plasminogen activator kringle-2 domain(1PK2), 18x20x18 points for plasminogen kringle-1 domain (4CIK), and 29x28x28 points for serine protease domain of plasminogen (5UGG) respectively. The grid was set up to encompass the active site pocket, with a spacing of 1 Å. The ligand hits were ranked according to their binding energies and finally, the best performing top ten ligands for each protein target were selected.

2.3.3. ParDOCK & Bappl+

The same set of 1500 hits (500 hits per protein) was screened by the Monte Carlo method involving an all-atom energy-based system using default parameters of ParDOCK software, hosted in the Sanjeevani server [41]. The ligands were positioned optimally around the active site of the protein target and ranked based on their interacting energies. Subsequently, the scoring function of all the aforementioned ligands was derived using the Bappl+ tool which utilizes the Random Forest algorithm scoring function [42]. In Bappl+ the default parameters were set and formal charges were assigned for each ligand. Based on these settings, the binding affinities of ligands were computed and the top ten compounds were ranked accordingly.

2.4. ADMET and TOPKAT

All the top ten identified ligands obtained by screening from Glide, Autodock Vina, ParDOCK, and Bappl+ tools were visually inspected in Pymol and Schrodinger maestro. Based on the docking scores, out of these ten identified ligands, the top three were selected for ADMET and TOPKAT (Toxicity Prediction by Computer Assisted Technology) analysis for each protein target. ADMET properties such as CYP2D6 & plasma protein inhibition, intestinal adsorption, aqueous solubility,

hepatotoxicity, blood-brain barrier level were evaluated using the Discovery studio 3.5 ADMET tool kit. Furthermore, Lipinski's rule of five was also checked for these ligands [43]. Thereafter, the toxicity of each ligand was estimated using the TOPKAT tool, which contains a robust Quantitative Structure-Toxicity Relationship (QSTR) modeling system to predict the accurate toxicity endpoints [44]. The toxicity properties such as rodent carcinogenicity, Ames mutagenicity, skin irritation, and developmental toxicity potential were also investigated.

2.5. Molecular Dynamics Simulation (MD)

The top three ranked ligands for each protein target were subjected to MD simulation using GROMACS (Groingen Machine for Chemical Simulations) 2019 suite implementing GROMOS (54a7) force field [45,46]. The protein-ligand complex was solvated in a cubic box of 0.8 nm using periodic boundary conditions and a Simple point-charge water model (SPCE) [47]. The Na+ and Cl- ions were added to neutralize the system and maintain the concentration of 0.15 mol/L. The PRODRG server was used to generate the ligand parameters and topology [48]. After that, internal constraints of the protein-ligand complex were relaxed by 2000 steps of steepest descent energy minimization with a max force constraint of 1000 KJ/mol, leading to restraining positions of all heavy atoms. Before MD simulations, the systems were heated using a V-rescale thermostat to attain the temperature of 310 K with 0.1ps as the constant of coupling and achieved equilibration in NVT (Number of atoms, Volume of the system, and Temperature of the system). Then solvent density was sustained using a Parrinello-Rahman barostat with the pressure of 1 bar, coupling constant of 0.1 ps, and temperature of 310 K to obtain equilibration in NPT (Number of atoms in the system, the pressure of the system, and temperature of the system) by gradually discharging the restraint on heavy atoms step by step [49]. Finally, an MD simulation was performed for the equilibrated structures for 5 ns with an integration time step of 2fs. The electrostatic interactions of long-range were implemented using particle-mesh Ewald sum with a cutoff of 1.0 nm [50]. During simulation, the LINCS algorithm was used to constrain all bond lengths, and the SETTLE algorithm was used for restraining water molecules [51-52]. The resultant structure from the NPT equilibration phase was employed for the final production run in the NPT ensemble for 200 ns simulation time. Finally, the trajectory analysis such as RMSD, RMSF, RoG, SASA, H-bonds, PCA of protein-ligand complexes was performed using gromacs utilities and plotted in xmgrace [53].

2.6. Principal Component Analysis

PCA is a statistical method that is applied to reduce data complexity and is useful for analyzing the large-scale motion of proteins [54]. Generally, internal motions of every protein molecule are ingrained and are required for their proper biological functioning like conformational changes to various biological environments, binding to substrate, etc. Due to problems in interpreting these internal motions of the protein, PCA is utilized to minimize the large dimensions of the data set to identify the prominent principal components (PCs). These PCs represent the major contributors responsible for elucidating crucial information about the dynamic changes of the protein. In PCA, a covariance matrix was constructed from trajectory data after eliminating unwanted motions (translational and rotational). This was followed by diagonalization of the covariance matrix using the gmx_covar tool which is a part of the Gromacs module. By diagonalization of covariance matrices containing backbone C alpha atoms data, the eigenvector and eigenvalues were obtained which corresponds to the change in protein trajectory throughout the simulation time. The *gmx anaeig* tool of Gromacs was used to analyze and plot the trajectories of the backbone C alpha atoms of all the systems. In our study, the first two projections (PC 1 and PC 2) with the highest eigenvalues were taken into consideration as they are responsible for 80–90% of the collective motions of the C alpha backbone atoms.

2.7. Free energy calculation

To evaluate the binding free energy (ΔG) of protein-ligand complexes, the Molecular Mechanics Poisson-Boltzmann Surface Area (MM-PBSA) method was employed [55]. We computed ΔG for the last 50ns of the production run using the *g_mmpbsa* tool of the Gromacs module [56]. Binding free energy was calculated for the identified ligands by estimating the bound and unbound state differences with the protein targets.

$$\Delta G_{binding} = G_{complex} - (G_{protein} + G_{ligand}) \longrightarrow (1)$$

In equation (1), the free energies of protein and ligands are indicated by $G_{protein}$ and G_{ligand}. The free energy of the protein-ligand complex is represented by the $G_{complex}$

$$G_x = (E_{MM}) - TS + (G_{solv}) \longrightarrow (2)$$

Similarly, equation (2) is used to calculate the bound or unbound state's free energy. The x indicates the unbound states or protein-ligand complex. E_{MM} is used to calculate the average molecular mechanics energy and TS indicates the entropic contribution. The solvation free energy is indicated by G_{solv}

$$E_{MM} = E_{bonded} + E_{nonbonded} \longrightarrow (3)$$

Equation (3) shows that bonded and non-bonded (i.e. vander Waal's & electrostatic) interactions were considered for calculating the molecular mechanics energy (E_{MM}) for protein-ligand interaction.

$$G_{solv} = G_{nonpolar} + G_{polar} \longrightarrow (4)$$

The linearized Poisson Boltzmann equation is represented by $G_{solv,}$ where polar and non-polar hydrophobic contribution (G_{polar} & $G_{nonpolar}$) is taken into consideration for estimating the solvent accessible surface area. It was assumed that as all ligands are binding to one distinct protein target, therefore these ligands will contribute similar entropic energy. Hence, in our analysis complicated entropic contribution was not taken into account and was removed at the time of calculation.

3. Results and discussion

3.1 Virtual screening (VS)

VS is the most widely used technique in the drug discovery process. The complete flow chart of our current study is represented in Figure 1. As mentioned earlier, we have selected three protein targets which known to play a crucial role in the fibrinolysis process i.e., tissue-type plasminogen activator kringle-2 domain (1PK2), plasminogen kringle-1 domain (4CIK), and serine protease domain of plasminogen (5UGG). From the crystallographic structures of protein i.e., 1PK2, 4CIK, and 5UGG, the co-crystallized ligands with ligand IDs ACA, XO3, and 89M were removed from the protein complex, and the residues found interacting with these ligands were selected as active site pockets. We have used the structure-based drug design approach to identify the lead compounds which could bind to the specific pocket region accordingly [57]. As mentioned earlier, one million molecules were retrieved from the ZINC database and post-screening of these compounds in the RASPD tool we obtained 500 hits for each protein target (1500 hits total). These

1500 compounds (500 per protein) were optimized in the Discovery studio and molecular docking was performed by three different tools accordingly.

3.2 Comparative Molecular Docking

To understand the interaction profile of 1500 ligands (500 per protein) with the protein targets, we conducted a comparative molecular docking analysis using three different tools, i.e., Auto dock Vina, Glide, and ParDOCK/BAPPL+. The 500 hits were individually docked to the active site pocket of 1PK2, 4CIK, and 5UGG respectively. The key active site residues of the 1PK2 protein target include TRP80, THR79, LEU78, ARG71, TRP69, ASP63, VAL40. Similarly, the binding site of the 4CIK protein target includes ARG35, ASP55, ASP57, TRP62, TYR64, ARG71, TYR72 active site residues. Likewise, for the 5UGG protein target, the residues selected for docking include PHE587, CYX588, HID603, LYS607, SER736, CYX737, GLN738, GLY739, SER741, THR759, TRP761, and GLY762. Based on the binding energies, the top 10 hits for each target protein were ranked based on the scores obtained from the three docking tools: Autodock vina, ParDOCK/BAPPL+, and Glide (Supplementary Table ST1, ST2, and ST3). Among these 10 hits, we narrowed it down to the top three ligands by selecting the common hits found in all three docking tools. The docking results obtained from docking all the nine identified ligands (P27, P67, P76, C19, C90, C97 U19, U94, U97) and the reference ligands (ACA, XO3, and 89M) with their respective protein targets (1PK2, 4CIK, and 5UGG) are provided in Table 1. Detailed Glide SP and XP scores of the top three ligands hit against each protein target are also provided in (Supplementary Table ST4). The interacting residues which include both the active site and novel (other than the active site) residues of the proteins (1PK2, 4CIK, and 5UGG) with their respective ligands (P27, P67, P76, C19, C90, C97 U19, U94, U97) 1PK2 are provided in Table 1. The 2D structures of the nine identified compounds (three for each protein target) are provided in Figure 2 [(A)-(I)]. As mentioned earlier, for comparative docking studies of the 1PK2 protein target, the ligand ACA was selected as the reference ligand. Its binding energy was found to be -3.9 kcal/mol and -4.9 kcal/mol in Autodock Vina and ParDOCK/BAPPL+ respectively. Similarly, the Glide score obtained for the reference ligand was -7.25 kcal/mol. Simultaneously, we conducted docking studies for each of the top three ligands i.e., ZINC12211330 (P27), ZINC00718625 (P67), ZINC09970930 (P76) against the 1PK2 protein target. The identified ligands P27, P67, P76 exhibited binding energy of -7.6, -8.3, -8.9 kcal/mol in Autodock Vina and -8.84, -9.60, -9.63

kcal/mol. in ParDOCK/ BAPPL+ respectively. Similarly, the Glide score obtained for P27, P67 & P76 was -8.6, -9.31, -9.42 kcal/mol respectively. As shown, the interacting residues of 1PK2 with P27 are LYS39, VAL40, TYR41, ASP63, TRP69, HIS71, ARG77, LEU78, THR79, TRP80, GLU81, TYR82. Likewise, the interacting residues of 1PK2 with P67 are GLU23, LYS39, VAL40, TYR41, HIS71, ASP63, TRP69, ARG77, LEU78, TRP80, GLU81, TYR82. Similarly, the interacting residues of 1PK2 with P76 are LYS39, VAL40, TYR41, TRP69, HIS71, ARG77, LEU78, THR79, TRP80, GLU81, TYR82. Docking studies for each of the top three ligands i.e., ZINC02060288 (C19), ZINC12455413 (C90), ZINC14888376 (C97) were performed against the 4CIK protein target. The identified ligands C19, C90, C97 exhibited binding energy of -8.2, -8.5, -8.8 kcal/mol in Autodock Vina and -8.90, -9.0, -9.47 kcal/mol in ParDOCK/ BAPPL+ respectively. Similarly, the Glide score obtained for C19, C90, C97 was -8.75, -8.92, -9.3 kcal/mol respectively. The reference ligand XO3 exhibited binding energy of -7.4 kcal/mol in Autodock Vina and - 6.66 kcal/mol in ParDOCK/BAPPL+ and -7.25 in Glide respectively. As shown, the interacting residues of 4CIK with C19 are ARG35, ASP55, ASP57, PRO58, GLN59, TRP62, TYR64, ARG71, TYR72, TYR74. Likewise, the interacting residues of 4CIK with C90 are ARG35, ASP55, ASP57, GLN59, TRP62, GLU69, LYS70, ARG71, TYR72, ASP73, TYR74. Similarly, the interacting residues of 4CIK with C97 are ARG35, PHE36, ASP55, ASP57, PRO58, GLN59, TRP62, TYR64, ARG71, TYR72, TYR74. In the same way, docking studies for each of the top three ligands i.e., ZINC12576410 (U19), ZINC04557820 (U94), ZINC11839443 (U97) were conducted against the 5UGG protein target. The identified ligands U19, U94 and U97 exhibited binding energy of -10.9, -11.0, -11.4 kcal/mol in Autodock Vina and -7.9, -8.02, -8.33 kcal/mol in ParDOCK/ BAPPL+ respectively. Similarly, the Glide score obtained for U19, U94, and U97 was -8.87, -9.41, -9.6 kcal/mol respectively. The reference ligand 89M exhibited binding energy of -9 kcal/mol in Autodock Vina and -5.9 kcal/mol in ParDOCK/BAPPL+ and -7.5 in Glide respectively. As shown, the interacting residues of 5UGG with U19 are HID63, CYS64, LEU65, GLU66, LYS67, SER68, ARG70, SER72, SER73, TYR74, GLN198, SER201. Likewise, the interacting residues of 5UGG with U94 are SER68, LYS67, TYR74, GLU66, LEU65, CYS64, HID63, CYS197, SER196, ASP195, VAL233, GLY232, CYS225, GLY224, LEU223, GLY222, TRP221, SER220, SER201. Similarly, the interacting residues of 5UGG with U97 are ALA62, HID63, CYS64, LEU65, GLU66, LYS67, SER68, TYR74, SER73, CYS197, SER196, ASP195, GLY232, VAL233, SER220, TRP221, GLY222, LEU223, GLY224, SER201. Overall, from the

docking results, it can be construed that in comparison to reference ligands ACA, XO3, and 89M, the identified ligands P27, P67, P76, C19, C90, C97 U19, U94, U97 exhibited higher binding energy and stronger affinity towards their respective protein targets 1PK2, 4CIK, and 5UGG. Apart from the active site residues of the target proteins, no other residues are found to interact with the reference ligand ACA, XO3, and 89M. Therefore, it can be ascertained that the identified ligands form more favorable interactions with their respective protein targets, thus enhancing stronger and stable binding. The 2D interaction images of all the top nine ligands P27, P67, P76, C19, C90, C97 U19, U94, U97 complexed with their respective protein targets 1PK2, 4CIK, and 5UGG are also provided in Figure 3 [(A)-(I)]. It is noteworthy to mention that out of the nine identified ligands, P76, C97, and U97 are the top three ligands that bind with greater affinity to their respective targets 1PK2, 4CIK, and 5UGG as implied from the docking scores obtained from Autodock vina, ParDOCK/BAPPL+ and Glide (Table1). Post docking, ADMET & TOPKAT properties such as solubility, intestinal adsorption, etc. of the identified ligands and the reference ligands were investigated, As provided in the supplementary table ST5 and ST6, these ligands were found non-hepatotoxic, have the least development toxicity and they don't inhibit the cytochrome 4502D6 (CYP2D6) enzyme. The discovered ligands were also found not to bind to Plasma Protein (PP) and to be free of carcinogenicity, mutagenicity, and skin irritation in rodents.

3.3 Molecular Dynamics Simulations

Molecular Dynamics Simulation (MDS) plays a significant role in studying conformational changes of protein-ligand complexes and provides valuable insights into the prediction and identification of protein-ligand interactions [58]. The top nine ligands P27, P67, P76, C19, C90, C97, U19, U94, U97 docked with their respective protein targets i.e., plasminogen activator kringle-2 domain (1PK2), plasminogen kringle-1 domain (4CIK), and serine protease domain of plasminogen (5UGG) were subjected to molecular dynamics simulation in GROMACS for 200ns duration. Also, MD simulation for 200ns was performed for reference ligands i.e., ACA, XO3, and 89M docked with 1PK2, 4CIK, and 5UGG respectively. Additionally, we performed a simulation run of 200ns for all the three proteins 1PK2, 4CIK, and 5UGG respectively without ligand (APO). Thereafter, we performed trajectory analysis such as Root-mean-square-deviation (RMSD), Root-mean-square fluctuation (RMSF), Radius of gyration (Rg), number of Hydrogen bonds, bond distribution, Principal component analysis (PCA), and binding free-energy calculation

(MMPBSA) for all the systems (standalone proteins, protein-reference ligand complex, and protein-identified ligand complex).

3.3.1 Root-mean-square deviation analysis

To elucidate the influence of ligands on the conformational stability of the protein, we have analyzed the root-mean-square deviation (RMSD) of backbone atoms of all the systems using the standard *g_rms* function of GROMACS for an overall time of 200 ns simulation run (Figure 4A-4C). As provided in supplementary table ST7**,** 1PK2 protein docked with the reference ligand ACA and the identified legends P27, P67, P76 shows an average deviation of 0.32± 0.04 nm, 0.45± 0.05 nm, 0.36± 0.04 nm, 0.4± 0.03 nm respectively. The 1PK2 APO protein exhibits an average deviation of 0.44± 0.05 nm. From the RMSD graphs, it can be inferred that all the systems are equilibrated and have converged within a range of 0.2-0.5nm (Figure 4A). Similarly, 4CIK protein docked with ligands X03 (reference ligand), C19, C90, C97 shows an average deviation of 0.29± 0.03 nm, 0.29± 0.03 nm, 0.3± 0.03 nm, 0.34± 0.04 nm respectively. The 4CIK APO protein exhibits an average deviation of 0.34± 0.06 nm. This suggests that all the systems are equilibrated and have converged within a range of 0.2 - 0.4 nm (Figure 4B, supplementary table ST7). Likewise, 5UGG protein docked with ligands 89M (reference ligand), U19, U94, U97 exhibited an average deviation of 0.24± 0.02 nm, 0.29± 0.02 nm, 0.3± 0.02 nm, 0.31± 0.02 nm respectively. The 5UGG APO protein shows deviations of 0.24± 0.02 nm. This implies that all the systems that have converged within a range of 0.2-0.35 nm have attained equilibration (Figure 4C, supplementary table ST7). Although the RMSD profile shows an insignificant difference in the average value and minor fluctuations throughout, convergence is observed which indicates that our simulations have achieved stable trajectories. Hence, other conformational dynamics analysis is required to deduce further conclusions.

3.3.2 Residue flexibility analysis

To understand the overall residue-wise protein dynamics in the systems, the evaluation of root mean square fluctuations (RMSF) plays a very important role. Therefore, to check the stability and flexibility of the residues, we have calculated the RMSFs for an entire simulation run of 200ns using the *gmx_rmsf* module of GROMACS (Figure 4D-4F). From the RMSF profile, it can be understood that 1PK2 protein docked with ligands P27, P67, P76 exhibited a similar pattern

of fluctuation like the reference ligand ACA at active site residues TRP80, THR79, LEU78, ARG 71, TRP69, ASP63 respectively. 1PK2 docked with ligands P27, P67 and P76 show a fluctuation peak of values 0.15nm, 0.16nm, 0.18nm at residue VAL40 respectively but a higher fluctuation peak of 0.36 nm is observed at residue VAL40 for the reference ligand. This indicates that the ligands P27, P67, P76 are contributing to greater rigidity to the binding pocket of 1PK2 (Figure 4D). Similarly, 4CIK protein docked with ligands C19, C90, C97 exhibited a similar pattern of fluctuation like the reference ligand XO3 at active site residues ARG35, TRP62, TYR64, ARG71, TYR72 respectively. Likewise, 4CIK docked with ligands C19, C90, C97 exhibited fluctuation of 0.15 nm at the residues ASP55, ASP57 but in the case of reference ligand XO3, a higher fluctuation of 0.3 nm is observed. Also, XO3 shows a higher peak of 0.42nm at residues ASN9 and LYS8. This suggests that the identified ligands C19, C90, C97 have made the binding pocket more rigid and intact (Figure 4E). In the same manner, 5UGG protein docked with ligands U19, U94, U97 displayed the fluctuation pattern resembling the reference ligand 89M at active site residues LYS67, PHE68, CYX83, HID87, GLN239 respectively. Likewise, 5UGG docked with ligands U19, U94, U97 exhibited fluctuation of 0.2nm, 0.2nm, 0.28nm at the residues GLY762, SER765, CYS763 respectively, but in the case of reference ligand 89M, a higher fluctuation of 0.32 nm is observed. Also, 89M shows a higher peak of 0.5nm at residues TRP736, THR737, and GLY738. This propounds that the identified ligands U19, U94, U97 have made the binding pocket more inflexible (Figure 4F). From the RMSF profile of all the systems, it can be inferred that the ligands P27, P67, P76, C19, C90, C97, U19, U94, U97 are responsible for the restricted dynamics at the active site residue pocket of their respective protein targets and for imparting structural rigidity.

3.3.3 Compactness analysis

To study the compactness of all the protein-ligand complexes, the radius of gyration (Rg) is computed using the *gmx_gyrate* function of GROMACS for a simulation time of 200ns. Rg is explained as the distance measured between the terminal end of protein and its center of mass during simulation. When a ligand docks to a protein, there is a conformational shift that changes the radius of gyration [59]. The compact protein structure tends to maintain a low Rg average deviation thus showing dynamic stability. The combined Rg plot of all ligands is represented in Figure 5A-5C. As provided in Figure 5A and supplementary table ST8, 1PK2 protein docked with

ligands ACA (reference ligand), P27, P67, P76 shows an average Rg deviation of 1.31± 0.02 nm, 1.29± 0.01 nm, 1.27± 0.01 nm, 1.28 ± 0.02 nm respectively from 30-200 ns simulation time. Similarly, 4CIK protein docked with ligands X03 (reference ligand), C19, C90, C97 shows an average Rg deviation of 1.26 ± 0.01 nm, 1.23± 0.01 nm, 1.22± 0.01 nm, 1.21 ± 0.01 nm respectively from 30-200 ns simulation time (Figure 5B and supplementary table ST8). Likewise, 5UGG protein docked with ligands 89M (reference ligand), U19, U94, U97 exhibited an average Rg deviation of 1.77± 0.01 nm, 1.74± 0.01 nm, 1.75± 0.01 nm, 1.73 ± 0.01 nm respectively from 30-200 ns simulation time (Figure 5C and supplementary table ST8). Collectively, from the radius of gyration profile, it can be concluded that the identified ligands P27, P67, P76, C19, C90, C97, U19, U94, U97 are responsible for making the structure more compact compared to the reference ligands ACA, XO3, and 89M respectively.

3.3.4 Solvent Accessible Surface Area analysis

To calculate the solvent-accessible surface area (SASA) of a molecular surface, a method is employed which involves the *in-silico* rolling of a spherical probe that approximates a water molecule, encompassing a full-atom protein model [60]. This procedure takes into account the expansion of the van der Waals radius for each atom by 1.4 Å (the radius of a polar solvent probe) followed by the calculation of the surface area of these atoms with expanded radius. Therefore, the SASA values of all the complexes were computed using the *gmx_sasa* function of GROMACS for a simulation time of 200ns (Figure 5D-5F).

As provided in Figure 5D and supplementary table ST9**,** 1PK2 protein docked with ligands ACA (reference ligand), P27, P67, P76 shows an average SASA value of 58.94± 1.7 $nm^{2,}$ 58.67± 1.83 nm^2, 58.34± 1.54 nm^2, 58.76± 1.53nm^2 respectively from 30-200 ns simulation timeframe. It is observed that the SASA curves followed the same trend as the reference ligand ACA. Similarly, 4CIK protein docked with ligands X03 (reference ligand), C19, C90, C97 shows an average SASA value of 54.46 ± 2.0 nm^2, 54.18± 2.3 nm^2, 54.28± 1.72 nm^2, 53.21± 1.7 nm^2 respectively from 30-200 ns simulation time frame (Figure 5E and supplementary table ST9). The C19, C90, C97 show a similar pattern of average SASA values when compared to XO3. Likewise, 5UGG protein docked with ligands 89M (reference ligand), U19, U94, U97 exhibited an average SASA value of 124.75± 2.85 $nm^{2,}$ 123.61± 2.36 nm^2, 124.32± 2.62 nm^2,124.24± 2.84 nm^2 respectively from 30-

200 ns simulation time frame (Figure 5F and supplementary table ST9). The same pattern of SASA values was obtained for all the identified ligands. It is observed that similar to reference ligands, the identified ligands make the active site residues of the protein targets readily accessible to the solvent surface, thus exposing the proteins to the hydration shell. Also, the SASA values obtained from the analysis of proteins docked with our identified ligands are found to be significantly similar to the reference protein-ligand complexes.

3.3.5 Hydrogen Bond and Bond distribution analysis

The hydrogen bonds (H-bonds) are known to play a key role in forming stable contacts between the ligands and protein target [61]. In this study, H-bond analysis was performed on all the protein-ligand systems for a total simulation run of 200ns. The number of H-bonds and their bond frequencies are plotted using the *gmx_hbond* tool of GROMACS and are represented in Figure 6A-6F. It is observed that the ligand P67 formed one stable H-bond of length 0.27 nm with the protein target 1PK2, and its frequency to form this bond is20 % (Figure 6A). Likewise, the P76 formed 2-3 H-bonds during the simulation period and its frequency to form a bond of length 0.28 nm is 17.5% (Figure 6A). Similarly, P27 had formed a bond of length 0.29 nm with a frequency of 17% (Figure 6A). The reference ligand ACA did not form stable H-bonds and the frequency to form a bond of length 0.28 nm is only 10% which is very less compared to identified ligands (Figure 6A). In the case of the 4CIK protein target, the ligand C97 established stable 1-2 H-bonds during the simulation period and had 23% frequency to form a bond of length 0.28nm (Figure 6B). In the same way, the C90 exhibited 1-2 H-bonds during the simulation period, and its ability to form a bond of length 0.27 is 18% (Figure 6B). Similarly, the ligand C19 formed 1 H-bond, and its frequency to form a bond of length 0.28 nm is 18% (Figure 6B). Lastly, we observed that the reference ligand XO3 formed unstable H-bonds during the simulation, and its frequency to form a bond of length 0.26 nm is only 10%, which is less compared to identified ligands (Figure 6B). Likewise, in the case of the 5UGG protein target, the ligand U97 formed 1-2 stable H-bonds during the simulation time, and its frequency to form a bond of length 0.27 nm is 22% (Figure 6C). The U94 ligand formed 2-4 stable H-bonds and the frequency to form a bond of length 0.27 nm is 27% (Figure 6C). Also, the ligand U19 formed 2-4 H-bonds, and its frequency to form a bond of length 0.28 nm is 20% (Figure 6C). Lastly, the reference ligand 89M formed 1-2 unstable H-bonds, and the frequency to form a bond of length 0.27 nm is 15% (Figure 6C). Overall, from the H-bond

analysis, it can be concluded that our identified ligands form stable and stronger H-bonds of length $\geq$ 0.28 nm with their target proteins compared to reference ligands.

3.3.6 Principal component analysis

In general, a protein-ligand complex that occupies a smaller phase space with a stable cluster denotes a highly stable complex [62]. Therefore, to explore this phenomenon, we have performed Principal Component Analysis (PCA) on the trajectories obtained from the 200ns simulation period for all the protein-ligand complexes as shown in the 2D plots of PCA (Figure 7A-7C). From the PCA graph of 1PK2, it is observed that the complexes formed by P27, P67, P76 with 1PK2 are clustered very closely and the area coverage is less compared to the reference ligand ACA (Figure 7A). In the same way, from the PCA graph of 4CIK, it is observed that the complexes formed by C19, C90, C97 with 4CIK are closely clustered and occupy less area compared to reference ligand XO3 (Figure 7B). Similarly, from the PCA graph of 5UGG, it is observed that the complexes formed by U19, U94, U97 with 5UGG are clustered and occupy small phase space compared to reference ligand 89M (Figure 7C). Thus, from the PCA analysis, it is implied that our identified ligands impart rigidity to their respective protein-ligand complexes by occupying smaller phase space with stable cluster formation compared to reference ligands.

3.3.7 Binding free energy calculation

The results obtained by calculation of the free energy of ligands give insights into ligands' binding potential with bonded and non-bonded entities [63]. In this study, the *g_mmpbsa* tool was used to calculate binding free energy (ΔG) for the last 50ns of the simulation time (Figure 7D-7F). From the MMPBSA graphs, it is observed that the reference ligand ACA, and the identified ligands P27, P67, P76 bound to 1PK2 target protein exhibit binding energy of -26.460 +/- 9.222 kJ/mol and -77.975 +/- 19.181 kJ/mol, -90.798 +/- 37.674 kJ/mol, -145.653 +/- 20.078 kJ/mol respectively (Figure 7D). Thus, the binding free energies (ΔG) of 1PK2 bound with our identified ligands were found to be significantly better than that of 1PK2 bound with the reference ligand. Additionally, the four individual energy components such as van der Waal energy (ΔE_{vdW}), electrostatic energy (ΔE_{elec}), polar solvation energy ($\Delta g_{polar\text{-}solv}$), and SASA energy ($\Delta G_{non\text{-}polar}$) were compared for all the four protein-ligand complexes i.e., 1PK2-ACA, 1PK2-P27, 1PK2-67 and 1PK2-P76. The details of the MMPBSA energies of all the protein-ligand complexes are provided in Table 2. As

provided in the table, the individual energy components van der Waal energy (ΔE_{vdW}), electrostatic energy (ΔE_{elec}), polar solvation energy ($\Delta G_{polar-solv}$) and SASA energy ($\Delta G_{non-polar}$) was found to be -40.822 +/ -9.960 kJ/mol, -5.951 +/- 6.304 kJ/mol, 27.127 +/- 13.044 kJ/mol, -6.815 +/- 1.117 kJ/mol in 1PK2-ACA complex, -118.529 +/- 17.130 kJ/mol, -5.881 +/- 6.590 kJ/mol, 61.449 +/- 21.931 kJ/mol, -15.014 +/- 1.943 kJ/mol in 1PK2-27 complex , -117.567 +/- 47.692 kJ/mol, -12.887 +/- 9.387 kJ/mol, 51.918 +/- 28.232 kJ/mol, -12.262 +/- 5.059 kJ/mol in 1PK2-67 complex and -171.612 +/- 24.161 kJ/mol, -0.102 +/- 3.913 kJ/mol, 42.307 +/- 10.310 kJ/mol, -16.246 +/- 2.225 kJ/mol kJ/mol in 1PK2-76 complex respectively. Similarly, from the MMPBSA graphs, it is observed that the reference ligand XO3 and the identified ligands C19, C90, C97 bound to the 4CIK protein target exhibit binding energy of -20.066 +/- 30.373 kJ/mol and -89.316 +/- 38.412 kJ/mol, -93.881 +/- 39.414 kJ/mol, -98.949 +/- 32.293 kJ/mol respectively (Figure 7E). The details of the energy components are provided in the table for all the four protein-ligand complexes i.e., 4CIK-XO3, 4CIK-C19, 4CIK-C90, and 4CIK-97. The ΔE_{vdW} component, the ΔE_{elec} component, the $\Delta G_{polar-solv}$ component and the $\Delta G_{non-polar}$ component was found to be -45.470 +/- 7.831 kJ/mol, -6.123 +/- 7.523 kJ/mol, 38.916 +/- 27.368 kJ/mol, -7.388 +/- 1.775 kJ/mol in 4CIK-XO3 complex, -178.135 +/- 49.112 kJ/mol, -19.139 +/- 11.123 kJ/mol, 126.667 +/- 27.807 kJ/mol, -18.703 +/- 4.933 kJ/mol in 4CIK-C19 complex , -178.135 +/- 49.112 kJ/mol, -8.939 +/- 11.123 kJ/mol, 111.896 +/- 27.807 kJ/mol, -18.703 +/- 4.933 kJ/mol in 4CIK-C90 complex, -128.666 +/- 35.350 kJ/mol, 0.790 +/- 3.810 kJ/mol, 41.817 +/- 25.156 kJ/mol, -12.890 +/- 3.743 kJ/mol in 4CIK-97 complex respectively. Likewise, from the MMPBSA graphs, it is observed that the reference ligand 89M and the identified ligands U19, U94, U97 bound to the 5UGG protein target, exhibits binding energy of -126.981 +/- 19.836 kJ/mol, and -217.150 +/- 16.376 kJ/mol, -168.674 +/- 20.963 kJ/mol, -238.846 +/- 17.788 kJ/mol respectively (Figure 7F). The ΔE_{vdW} component, the ΔE_{elec} component, the $\Delta G_{polar-solv}$ component and the $\Delta G_{non-polar}$ component was found to be -199.690 +/- 9.099 kJ/mol, -30.462 +/- 10.217 kJ/mol, 126.314 +/- 23.798 kJ/mol, -23.143 +/- 1.662 kJ/mol in 5UGG-89M complex, -326.449 +/- 12.469 kJ/mol, -28.751 +/- 14.338 kJ/mol, 164.799 +/- 11.051 kJ/mol, -26.749 +/- 0.969 kJ/mol in 5UGG-U19 complex, -193.346 +/- 18.772 kJ/mol. -24.924 +/- 13.795 kJ/mol, 106.994 +/- 23.339 kJ/mol, -17.398 +/- 1.411 kJ/mol in 5UGG-U94 complex, -332.423 +/- 12.146 kJ/mol, -28.614 +/- 7.827 kJ/mol, 148.128 +/- 10.778 kJ/mol, -25.937 +/- 1.160 kJ/mol in 5UGG-U97 complex respectively. The 3D images of the top nine identified ligands

P27, P67, P76, C19, C90, C97, U19, U94, U97 bound to the active site residues of their respective protein targets 1PK2, 4CIK, and 5UGG are shown in supplementary figure 1 [(A)-(I)]. Furthermore, from the binding energy calculation, it can also be concluded that out of the nine identified ligands, the top three ligands having the best binding energy are P76, C97, and U97 against their protein targets 1PK2, 4CIK, and 5UGG respectively. The 3D images of these top three ligands P76, C97, and U97 bound to the active site residues of their respective protein targets 1PK2, 4CIK, and 5UGG are shown in Figure 8 [(A)-(C)]. From the MMPBSA profile, it can be inferred that the identified ligands docked with their respective target protein have the highest electrostatic energy, SASA energy, and Vander Waal energy in comparison with reference ligands. This also indicates that despite intermittent hydrogen bond formations as observed during h-bond analysis, the ligands were conserved in the binding pocket by nonbonded interactions (electrostatic, polar, and nonpolar). Based on overall MD analysis and MMPBSA energies, we have found the ligands P76, C97. and U97 to be the best performing amongst the top nine ligands.

4. Conclusions

In this study, we have identified compounds that can inhibit fibrinolysis by targeting each of the three important protein domains: the kringle-2 domain of tissue-type plasminogen activator, the kringle-1 domain of plasminogen, and the serine protease domain of plasminogen respectively. The top nine ligands (P27, P67, P76, C19, C90, C97, U19, U94, U97) were obtained by screening one million molecules from the Zinc database. These ligands were docked to their respective protein targets (1PK2, 4CIK, and 5UGG) using Autodock-Vina, Schrodinger-Glide, and ParDOCK/BAPPL+. Docking scores of these top nine ligands were evaluated and their ADMET profiling was also performed keeping the reported ligands (ACA, XO3, and 89M) as reference. All the top nine ligands, with the best scores and good ADMET results, were individually subjected to MD simulation for a period of 200 ns followed by detailed trajectory analysis. RMSD profile suggests that all the protein-ligand complexes have attained stable trajectories and are well equilibrated. From the RMSF analysis of all the systems, it can be inferred that the identified ligands are responsible for the restricted dynamics at the active site residue pocket of their respective protein targets, thereby imparting structural rigidity to the protein compared to the reference ligands. Rg data of all the systems reveals that in comparison to reference ligands, our identified ligands contribute greater compactness to the structure of their respective protein targets.

From the SASA analysis, it is evident that similar to reference ligands, the identified ligands make the active site residues of the protein targets well exposed to the solvent, thereby making them readily accessible. From the h-bond analysis and bond distribution, it was observed that the identified ligands tend to form stronger H-bonds of length $\geq$ 0.28 nm with their target proteins compared to reference ligands. PCA analysis helps us to understand that in comparison to reference ligands our identified ligands occupy smaller phase space and form stable clusters, thus conferring more stability to the protein-ligand complexes. The results obtained by analyzing molecular docking and MD simulation data are well-validated by the binding free energy calculation. From the MMPBSA profile, it is observed that, in the identified protein-ligand complexes, there exist strong interactions in terms of energy components other than hydrogen bonding such as electrostatic energy, SASA energy, and Vander Waal energy compared to reference protein-ligand complexes. Based on overall MD analysis and MMPBSA energies, we have found the ligands P76, C97, and U97 to be the best performing amongst the top nine ligands. Hence, our study strongly substantiates the point that our identified ligands can act as strong inhibitors and further experimental studies can be conducted to prove the therapeutic potential of these promising antifibrinolytic agents.

References

[1] J.C. Chapin, K.A. Hajjar, Fibrinolysis and the control of blood coagulation, Blood Rev. 29 (2015) 17-24. https://doi.org/10.1016/J.BLRE.2014.09.003.

[2] P. Harpel, T. Chang, E. Verderber., Tissue plasminogen activator and urokinase mediate the binding of Glu-plasminogen to plasma fibrin I. Evidence for new binding sites in plasmin-degraded fibrin, J. Biol. Chem. 260(1985) 4432-4440. https://doi.org/10.1016/S0021-9258(18)89283-3

[3] R. Fears, Binding of plasminogen activators to fibrin: characterization and pharmacological consequences. Biochem J. 261(1989):313-24. https://doi.org/10.1042/bj2610313

[4] V. V Novokhatnys, K.C. Inghams, L. V Medveds, Domain Structure and Domain-Domain Interactions of Recombinant Tissue Plasminogen Activator, J. Biol. Chem. 266 (1991) 12994–13002. https://doi.org/10.1016/S0021-9258(18)98794-6.

[5] J.H. Verheijen, M.P. Caspers, G.T. Chang, G.A. de Munk, P.H. Pouwels, B.E. Enger-Valk, Involvement of finger domain and kringle 2 domain of tissue-type plasminogen activator in fibrin binding and stimulation of activity by fibrin., EMBO J. 5 (1986) 3525. https://doi.org/10.1002/j.1460-2075.1986.tb04678.x.

[6] T.K. Korhonen, J. Haiko, L. Laakkonen, H.M. Järvinen, B. Westerlund-Wikström, Fibrinolytic and coagulative activities of Yersinia pestis, Front. Cell. Infect. Microbiol. 3 (2013). https://doi.org/10.3389/FCIMB.2013.00035.

[7] H.R. Lijnen, M. Hoylaerts, D. Collen, Isolation and characterization of a human plasma protein with affinity for the lysine binding sites in plasminogen. Role in the regulation of fibrinolysis and identification as histidine-rich glycoprotein, J. Biol. Chem. 255 (1980) 10214–10222. https://doi.org/10.1016/S0021-9258(19)70451-7.

[8] D. Ayón-Núñez, G. Fragoso, RJ Bobes, JP Laclette, Plasminogen-binding proteins as an evasion mechanism of the host's innate immunity in infectious diseases, Bioscience Reports. (2018) 31;38(5) https://doi.org/10.1042/BSR20180705

[9] MJ Colomina, E. Méndez, A. Sabate, Altered fibrinolysis during and after surgery, Thieme-Connect.Com. 47 (2021) 512–519. https://doi.org/10.1055/s-0041-1722971.

[10] P.L. McCormack, Tranexamic acid: a review of its use in the treatment of hyperfibrinolysis, Drugs. 72 (2012) 585–617. https://doi.org/10.2165/11209070-000000000-00000.

[11] T. Nishida, T. Kinoshita, K. Yamakawa, Tranexamic acid and trauma-induced coagulopathy, J. Intensive Care. 5 (2017). https://doi.org/10.1186/S40560-016-0201-0.

[12] I. Roberts, H. Shakur, T. Coats, B. Hunt, E. Balogun, L. Barnetson, L. Cook, T. Kawahara, P. Perel, D. Prieto-Merino, M. Ramos, J. Cairns, C. Guerriero, The CRASH-2 trial: a randomised controlled trial and economic evaluation of the effects of tranexamic acid on death, vascular occlusive events and transfusion requirement in bleeding trauma patients, Health Technol. Assess. 17 (2013) 1–80. https://doi.org/10.3310/HTA17100.

[13] G.R.W. Hunter, G.B. Young, Seizures After Cardiac Surgery, J. Cardiothorac. Vasc. Anesth. 25 (2011) 299–305. https://doi.org/10.1053/J.JVCA.2010.08.004.

[14] A. Ockerman, T. Vanassche, M. Garip, C. Vandenbriele, M.M. Engelen, J. Martens, C. Politis, R. Jacobs, P. Verhamme, Tranexamic acid for the prevention and treatment of bleeding in surgery, trauma and bleeding disorders: a narrative review, Thromb. J. 19 (2021) 54. https://doi.org/10.1186/S12959-021-00303-9.

[15] M. Mortensen, J. Krall, K.T. Kongstad, B.M. Brygger, O. Lenzi, P. Francotte, T.E. Sørensen, B. Nielsen, A.A. Jensen, T.G. Smart, B. Frølund, Developing New 4-PIOL and 4-PHP Analogues for Photoinactivation of γ-Aminobutyric Acid Type A Receptors, ACS Chemical Neuroscience. 10 (2019) 4669–4684. https://doi.org/10.1021/acschemneuro.9b00478.

[16] R.H.P. Law, G. Wu, E.W.W. Leung, K. Hidaka, A.J. Quek, T.T. Caradoc-Davies, D. Jeevarajah, P.J. Conroy, N.M. Kirby, R.S. Norton, Y. Tsuda, J.C. Whisstock, X-ray crystal structure of plasmin with tranexamic acid-derived active site inhibitors, Blood Adv. 1 (2017) 766–771. https://doi.org/10.1182/bloodadvances.2016004150.

[17] B. Wiman, D.Collen. Nature, Molecular mechanism of physiological fibrinolysis,

Nature.Com. 272(5653):549-50 (1978). https://doi.org/10.1038/272549a0.

[18] A.-J. Van Zonneveld, H. Veerman, H. Pannekoeks, On the Interaction of the Finger and the Kringle-2 Domain of Tissue-type Plasminogen Activator with Fibrin INHIBITION OF KRINGLE-2 BINDING TO FIBRIN BY t-AMINO CAPROIC ACID, J. Biol. Chem 261 (1986) 14214–14218. https://doi.org/10.1016/S0021-9258(18)67006-1.

[19] F.J. Castellino, S.G. McCance, The kringle domains of human plasminogen, Ciba Found. Symp. 212 (1997) 46–65. https://doi.org/10.1002/9780470515457.CH4.

[20] C.B. Keragala, R.L. Medcalf, Plasminogen: an enigmatic zymogen, Blood. 137 (2021) 2881–2889. https://doi.org/10.1182/blood.2020008951.

[21] E. Lionta, G. Spyrou, D K Vassilatis, Z. Cournia, Structure-based virtual screening for drug discovery: principles, applications and recent advances. Current topics in medicinal chemistry. 1;14(2014) 1923-38.DOI:10.2174/1568026614666140929124445

[22] I. Byeon, M. Llinás, Solution structure of the tissue-type plasminogen activator kringle 2 domain complexed to 6-aminohexanoic acid an antifibrinolytic drug, J. Mol. Biol. Elsevier. 222(1991):1035-51 https://doi.org/10.1016/0022-2836(91)90592-T

[23] L. Cheng, D. Pettersen, B. Ohlsson, P. Schell, M. Karle, E. Evertsson, S. Pahlén, M. Jonforsen, A.T. Plowright, J. Boström, T. Fex, A. Thelin, C. Hilgendorf, Y. Xue, G. Wahlund, W. Lindberg, L.O. Larsson, D. Gustafsson, Discovery of the fibrinolysis inhibitor AZD6564, acting via interference of a protein-protein interaction, ACS Med. Chem. Lett. 5 (2014) 538–543. https://doi.org/10.1021/ML400526D.

[24] R. Law, G. Wu, E. Leung, K. Hidaka, AJ Quek, TT Caradoc-Davies, D. Jeevarajah, PJ Conroy, NM Kirby, RS Norton, Y. Tsuda, X-ray crystal structure of plasmin with tranexamic acid–derived active site inhibitors. Blood advances. (2017):766-71. https://doi.org/10.1182/bloodadvances.2016004150

[25] H.M. Berman, J. Westbrook, Z. Feng, G. Gilliland, T.N. Bhat, H. Weissig, I.N. Shindyalov,

P.E. Bourne, The Protein Data Bank, Nucleic Acids Res. 28 (2000) 235–242. https://doi.org/10.1093/NAR/28.1.235.

[26] The PyMOL Molecular Graphics System, Version 2.0 Schrödinger, LLC.

[27] B. Webb, A. Sali, Comparative protein structure modeling using MODELLER, Curr. Protoc. Bioinforma. 2016 (2016) 5.6.1-5.6.37. https://doi.org/10.1002/CPBI.3.

[28] Systemes, D. BIOVIA. "Discovery Studio Modeling Environment." Dassault Systèmes, San Diego (2016).

[29] B.R. Brooks, C.L. Brooks, A.D. Mackerell, L. Nilsson, R.J. Petrella, B. Roux, Y. Won, G. Archontis, C. Bartels, S. Boresch, A. Caflisch, L. Caves, Q. Cui, A.R. Dinner, M. Feig, S. Fischer, J. Gao, M. Hodoscek, W. Im, K. Kuczera, T. Lazaridis, J. Ma, V. Ovchinnikov, E. Paci, R.W. Pastor, C.B. Post, J.Z. Pu, M. Schaefer, B. Tidor, R.M. Venable, H.L. Woodcock, X. Wu, W. Yang, D.M. York, M. Karplus, CHARMM: The Biomolecular Simulation Program, J. Comput. Chem. 30 (2009) 1545. https://doi.org/10.1002/JCC.21287.

[30] T. Sterling, J.J. Irwin, ZINC 15 - Ligand Discovery for Everyone, J. Chem. Inf. Model. 55(2015)2324–2337. https://doi.org/10.1021/acs.jcim.5b00559.

[31] G. Mukherjee, B. Jayaram, A rapid identification of hit molecules for target proteins via physico-chemical descriptors, Phys. Chem. Chem. Phys. 15 (2013) 9107–9116. https://doi.org/10.1039/C3CP44697B.

[32] O. Trott, A.J. Olson, AutoDock Vina: improving the speed and accuracy of docking with a new scoring function, efficient optimization, and multithreading, J. Comput. Chem. 31 (2010) 455–461. https://doi.org/10.1002/jcc.21334.

[33] Glide version 6.2. (2019). New York, NY: Schrodinger, LLC.

[34] A. Gupta, P. Sharma, B. Jayaram, ParDOCK: An All Atom Energy Based Monte Carlo Docking Protocol for Protein-Ligand Complexes, Protein Pept. Lett. 14 (2007) 632–646. https://doi.org/10.2174/092986607781483831.

[35] A. Soni, R. Bhat, B. Jayaram, Improving the binding affinity estimations of protein–ligand complexes using machine-learning facilitated force field method, J. Comput. Aided. Mol. Des. 34 (2020) 817–830. https://doi.org/10.1007/S10822-020-00305-1.

[36] LigPrep, version 2.9. (2013). New York, NY: Schrodinger, LLC.

[37] R.A. Friesner, R.B. Murphy, M.P. Repasky, L.L. Frye, J.R. Greenwood, T.A. Halgren, P.C. Sanschagrin, D.T. Mainz, Extra precision glide: Docking and scoring incorporating a model of hydrophobic enclosure for protein− ligand complexes, J. med. Chem. ACS Publ. 49 (2006) 6177–6196. https://doi.org/10.1021/jm051256o.

[38] R.A. Friesner, J.L. Banks, R.B. Murphy, T.A. Halgren, J.J. Klicic, D.T. Mainz, M.P. Repasky, E.H. Knoll, M. Shelley, J.K. Perry, D.E. Shaw, P. Francis, P.S. Shenkin, Glide: A New Approach for Rapid, Accurate Docking and Scoring. 1. Method and Assessment of Docking Accuracy, J. Med. Chem. 47 (2004) 1739–1749. https://doi.org/10.1021/JM0306430.

[39] N.M. O'Boyle, M. Banck, C.A. James, C. Morley, T. Vandermeersch, G.R. Hutchison, Open Babel: An Open chemical toolbox, J. Cheminform. 3 (2011) 1–14. https://doi.org/10.1186/1758-2946-3-33

[40] P.A. Kollman, I. Massova, C. Reyes, B. Kuhn, S. Huo, L. Chong, M. Lee, T. Lee, Y. Duan, W. Wang, O. Donini, P. Cieplak, J. Srinivasan, D.A. Case, T.E. Cheatham, Calculating structures and free energies of complex molecules: combining molecular mechanics and continuum models, Accounts of chemical research. ACS Publ. 33 (2000) 889–897. https://doi.org/10.1021/ar000033j.

[41] B. Jayaram, T. Singh, G. Mukherjee, A. Mathur, S. Shekhar, V. Shekhar, Sanjeevini: a freely accessible web-server for target directed lead molecule discovery., BMC Bioinformatics. 13 Suppl 1 (2012) 1–13. https://doi.org/10.1186/1471-2105-13-S17-S7

[42] H. Li, K. Leung, MH. Wong, PJ Ballester, Improving AutoDock Vina using random forest: the growing accuracy of binding affinity prediction by the effective exploitation of larger data sets, Molecular informatics Wiley Online Libr. 34 (2015) 115–126.

https://doi.org/10.1002/minf.201400132.

[43] CA. Lipinski Lead-and drug-like compounds: the rule-of-five revolution. Drug discovery today:Technologies.1(2004):337-41.https://doi.org/10.1016/j.ddtec.2004.11.007

[44] MJ. Prival. Evaluation of the TOPKAT system for predicting the carcinogenicity of chemicals. Environmental and molecular mutagenesis. 2001;37(1):55-69..

[45] S. Pronk, S. Páll, R. Schulz, P. Larsson, R. Apostolov, MR. Shirts, JC Smith, PM Kasson, D. Van Der Spoel, B. Hess, GROMACS 4.5: a high-throughput and highly parallel open-source molecular simulation toolkit. Bioinformatics.29(2013):845-54. https://doi.org/10.1093/bioinformatics/btt055

[46] W. Huang, Z. Lin, W.F. Van Gunsteren, Validation of the GROMOS 54A7 force field with respect to β-peptide folding, J. Chem. Theory Comput. 7 (2011) 1237–1243. https://doi.org/10.1021/CT100747Y.

[47] J. Zielkiewicz, Structural properties of water: Comparison of the SPC, SPCE, TIP4P, and TIP5P models of water, J. Chem. Phys. 123 (2005). https://doi.org/10.1063/1.2018637.

[48] AW Schuttelkopf, DM Van Aalten, PRODRG: a tool for high-throughput crystallography of protein–ligand complexes. Acta Crystallogr. D 60(2004):1355-63. https://doi.org/10.1107/S0907444904011679

[49] M. Parrinello, A. Rahman, Polymorphic transitions in single crystals: A new molecular dynamics method, J. Applied phy. 52 (1981) 7182. https://doi.org/10.1063/1.328693.

[50] U. Essmann, L. Perera, ML. Berkowitz, T. Darden, H. Lee, LG Pedersen, A smooth particle mesh Ewald method. J. chem. phy. 103(1995):8577-93. https://doi.org/10.1063/1.470117

[51] B. Hess, H. Bekker, H.J.C. Berendsen, J.G.E.M. Fraaije, LINCS: A Linear Constraint Solver for Molecular Simulations, J Comput Chem. 18 (1997) 14631472. https://doi.org/10.1002/(SICI)1096-987X(199709)18:12.

[52] S. Miyamoto, P.A. Kollman, Settle: An analytical version of the SHAKE and RATTLE

algorithm for rigid water models, J. Comput. Chem. 13 (1992) 952–962. https://doi.org/10.1002/JCC.540130805.

[53] Turner PJ. XMGRACE, Version 5.1. 19. Center for Coastal and Land-Margin Research, Oregon Graduate Institute of Science and Technology, Beaverton, OR. 2005;2.

[54] C.C. David, D.J. Jacobs, Principal component analysis: A method for determining the essential dynamics of proteins, Methods Mol. Biol. 1084 (2014) 193–226. https://doi.org/10.1007/978-1-62703-658-0_11.

[55] S. Genheden, U. Ryde. The MM/PBSA and MM/GBSA methods to estimate ligand-binding affinities, Expert opinion on drug discovery 10 (2015) 449–461. https://doi.org/10.1517/17460441.2015.1032936.

[56] R. Kumari, R.Kumar, g_mmpbsa A GROMACS Tool for High-Throughput MM-PBSA Calculations, J. Chem. Inf. Model ACS Publ. 54 (2014) 1951–1962. https://doi.org/10.1021/ci500020m.

[57] AC Anderson, The process of structure-based drug design, Chemistry & biology Elsevier.10(2003):787-97. https://doi.org/10.1016/j.chembiol.2003.09.002

[58] J.D. Durrant, J.A. McCammon, Molecular dynamics simulations and drug discovery, BMC Biol. 9 (2011). https://doi.org/10.1186/1741-7007-9-71.

[59] D. Seeliger, B.L. De Groot, Conformational transitions upon ligand binding: Holo-structure prediction from apo conformations, PLoS Comput. Biol. 6 (2010). https://doi.org/10.1371/JOURNAL.PCBI.1000634.

[60] E. Durham, B. Dorr, N. Woetzel, R. Staritzbichler, J. Meiler, Solvent accessible surface area approximations for rapid and accurate protein structure prediction, J. Mol. Model. 15 (2009) 1093–1108. https://doi.org/10.1007/S00894-009-0454-9.

[61] D. Chen, N. Oezguen, P. Urvil, C. Ferguson, S.M. Dann, T.C. Savidge, Regulation of protein-ligand binding affinity by hydrogen bond pairing, Science advances 2 (2016). https://doi.org/10.1126/sciadv.1501240.

[62] E. Papaleo, P. Mereghetti, P. Fantucci, R. Grandori, L. De Gioia, Free-energy landscape, principal component analysis, and structural clustering to identify representative conformations from molecular dynamics simulations: the myoglobin case. J. Mol. Graph. Model. (2009):889-99. https://doi.org/10.1016/j.jmgm.2009.01.006

[63] C. Wang, D. Greene, L. Xiao, R. Qi, R. Luo, Recent developments and applications of the MMPBSA method, Front. Mol. Biosci. 4 (2018) 87. https://doi.org/10.3389/FMOLB.2017.00087/BIBTEX.

Statement of conflict of interests

The authors state that they have no conflicts of interest.

Authorship Contribution

Suparna Banerjee: Investigation, Data curation, Formal analysis, Validation, Visualization, Writing - original draft, review& editing. Yeshwanth M.: Investigation, Data curation, Formal analysis, Validation, Visualization, Writing - original draft, review& editing. D. Prabhu: Data curation, Formal analysis (GLIDE), K. Sekar: Supervision, Prosenjit Sen: Conceptualization, Supervision, Writing - review& editing. Suparna Banerjee and Yeshwanth M. have contributed equally to the work.

Acknowledgments

The authors owe sincere thanks to the Department of Science and Technology, Government of India, and Indian Association for the Cultivation of Science, Kolkata, India for providing all the necessary facilities. The authors acknowledge the HPC facilities offered by the centre of excellence in structural biology and bio-computing funded by the Department of Biotechnology, Government of India, and the Department of Computational and Data Sciences, Indian Institute of Science, Bangalore, India. Suparna Banerjee gratefully acknowledges the support of the Council of Scientific & Industrial Research, Govt. of India for fellowship.

Figure 1: Flow chart of the virtual screening process using combined molecular docking and molecular dynamics simulation approaches.

Figure 2: The 2D structures of the lead identified compounds (A) ZINC12211330 (P27), (B) ZINC00718625 (P67), (C) ZINC09970930 (P76), (D) ZINC02060288 (C19), (E) ZINC12455413 (C90), (F) ZINC14888376 (C97), (G) ZINC12576410 (U19), (H) ZINC04557820 (U94), (I) ZINC11839443 (U97)

Figure 3: The 2D interaction profile of lead molecules into the binding site of their respective protein targets 1PK2, 4CIK and 5UGG (A) ZINC12211330 (P27), (B) ZINC00718625 (P67), (C) ZINC09970930 (P76), (D) ZINC02060288 (C19), (E) ZINC12455413 (C90), (F) ZINC14888376 (C97), (G) ZINC12576410 (U19), (H) ZINC04557820 (U94), (I) ZINC11839443 (U97)

Figure 4: (A) RMSD profile of 1PK2 protein-ligand complexes (top three identified ligands P27, P67, P76, and reference ligand ACA) along with APO. (B) RMSD profile of 4CIK protein-ligand complexes (top three identified ligands C19, C90, C97and reference ligand XO3) along with APO. (C) RMSD profile of 5UGG protein-ligand complexes (top three identified ligands U19, U94, U97, and reference ligand 89m) along with APO. (D) RMSF profile of 1PK2 protein-ligand complexes (top three identified ligands P27, P67, P76, and reference ligand ACA) along with APO. (E) RMSF profile of 4CIK protein-ligand complexes (top three identified ligands C19, C90, C97and reference ligand XO3) along with APO. (F) RMSF profile of 5UGG protein-ligand complexes (top three identified ligands U19, U94, U97 and reference ligand 89m) along with APO.

Figure 5: (A) Radius of gyration profile of 1PK2 protein-ligand complexes (top three identified ligands P27, P67, P76, and reference ligand ACA) along with APO. (B) The radius of gyration profile of 4CIK protein-ligand complexes (top three identified ligands C19, C90, C97and reference ligand XO3) along with APO. (C) The radius of gyration profile of 5UGG protein-ligand complexes (top three identified ligands U19, U94, U97, and reference ligand 89m) along with APO. (D) SASA profile of 1PK2 protein-ligand complexes (top three identified ligands P27, P67, P76, and reference ligand ACA) along with APO. (E) SASA profile of 4CIK protein-ligand complexes (top three identified ligands C19, C90, C97and reference ligand XO3) along with APO. (F) SASA profile of 5UGG protein-ligand complexes top three identified ligands U19, U94, U97 and reference ligand 89m) along with APO.

Figure 6: (A) Hydrogen bonding pattern of 1PK2 protein-ligand complexes (top three identified ligands P27, P67, P76, and reference ligand ACA) along with APO. (B) Hydrogen bonding pattern of 4CIK protein-ligand complexes (top three identified ligands C19, C90, C97and reference ligand XO3) along with APO. (C) Hydrogen bonding pattern of 5UGG protein-ligand complexes (top three identified ligands U19, U94, U97, and reference ligand 89m) along with APO. (D) H-Bond frequencies of 1PK2 protein-ligand complexes (top three identified ligands P27, P67, P76, and reference ligand ACA) along with APO. (E) H-Bond frequencies of 4CIK protein-ligand complexes (top three identified ligands C19, C90, C97 and reference ligand XO3) along with APO. (F) H-Bond frequencies of 5UGG protein-ligand complexes top three identified ligands U19, U94, U97 and reference ligand 89m) along with APO.

Figure 7: Principal component analysis and MMPBSA analysis. (A)Projection of motion of Apo-1PK2 in black; 1PK2-ACA complex in yellow; 1PK2-P27 complex in red; 1PK2-P67 in green; 1PK2-P76 in blue. (B) Projection of motion of Apo-4CIK in black; 4CIK-XO3 complex in yellow; 4CIK -C19 complex in red; 4CIK -C90 in green; 4CIK-C97 in blue. (C) Projection of motion of Apo-5UGG in black; 5UGG-89M complex in yellow; 5UGG -U19 complex in red; 5UGG -U94 in green; 5UGG -U97 in blue. (D) Binding energy profile (ΔG) of 1PK2 complexed with the identified ligands P27, P67, P76, and reference ligand ACA. (E) Binding energy profile (ΔG) of 4CIK complexed with the identified ligands C19, C90, C97, and reference ligand XO3. (F) Binding energy profile (ΔG) of 5UGG complexed with the identified ligands U19, U94, U97, and reference ligand 89M.

Figure 8: Schematic representation of the top three identified ligands docked to the active site residues of their respective protein targets using VMD. (A) P76 bound to 1PK2 (B) C97 bound to 4CIK (C) U97 bound to 5UGG. Proteins are shown in the New Cartoon representation. Active site residues of the proteins are shown in licorice representation. Identified ligands are shown in CPK representation.

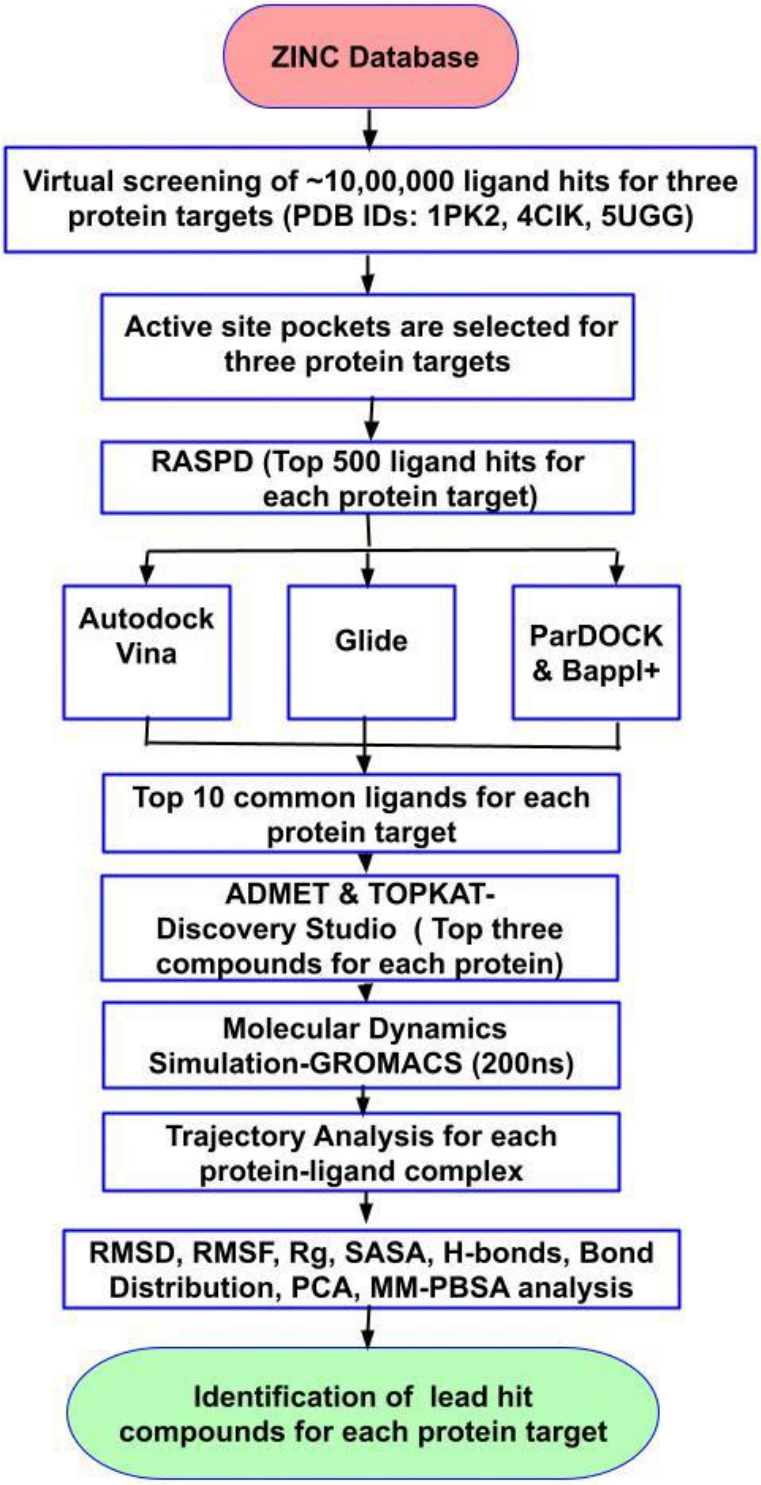
ZINC Database
Virtual screening of ~10,00,000 ligand hits for three protein targets (PDB IDs: 1PK2, 4CIK, 5UGG)
Active site pockets are selected for three protein targets
RASPD (Top 500 ligand hits for each protein target)
Autodock Vina
Glide
ParDOCK & Bappl+
Top 10 common ligands for each protein target
ADMET & TOPKAT-Discovery Studio (Top three compounds for each protein)
Molecular Dynamics Simulation-GROMACS (200ns)
Trajectory Analysis for each protein-ligand complex
RMSD, RMSF, Rg, SASA, H-bonds, Bond Distribution, PCA, MM-PBSA analysis
Identification of lead hit compounds for each protein target

Figure 1

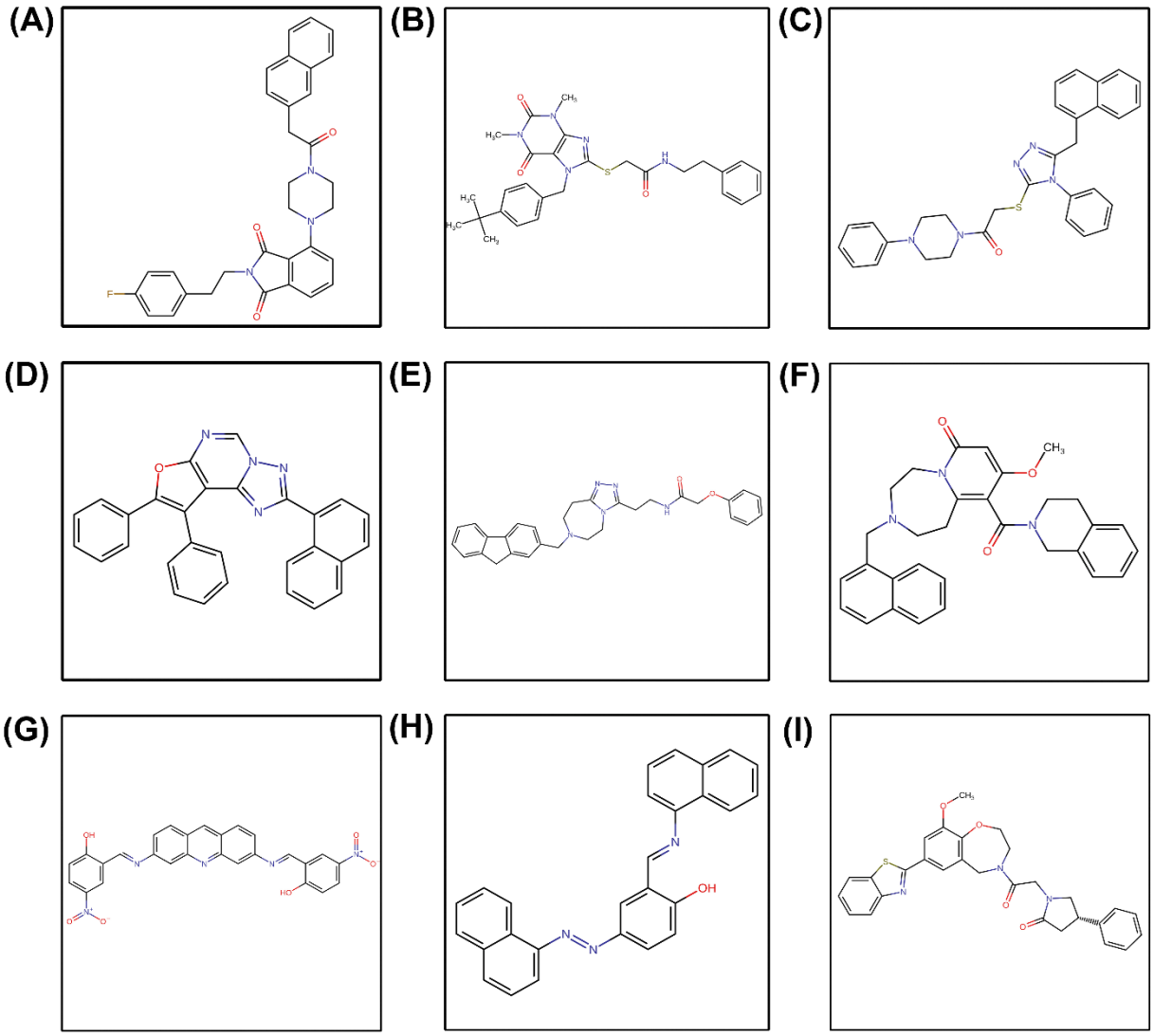

Figure 2

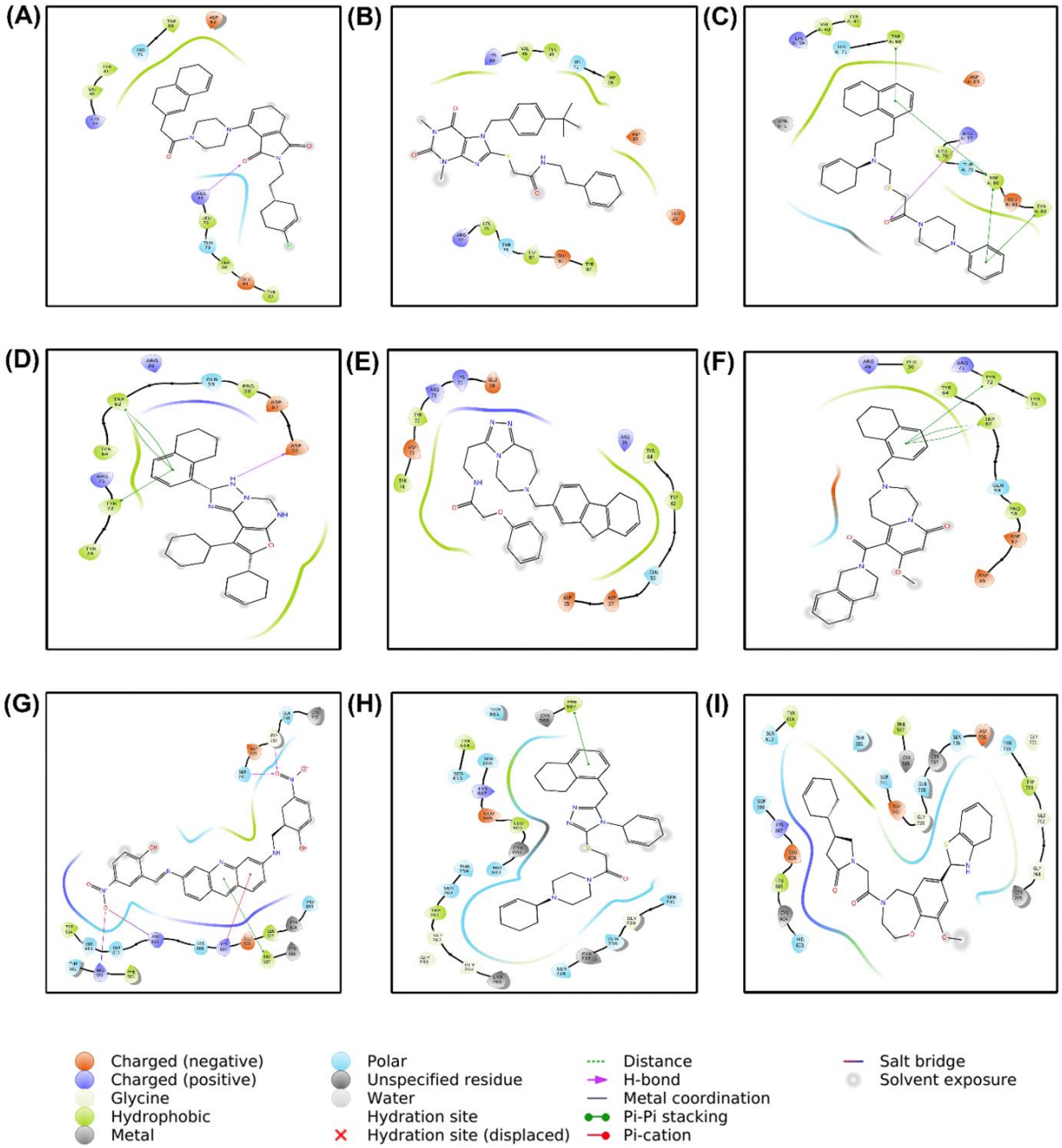
(A)
(B)
(C)
(D)
(E)
(F)
(G)
(H)
(I)
Charged (negative)
Charged (positive)
Glycine
Hydrophobic
Metal
Polar
Unspecified residue
Water
Hydration site
Hydration site (displaced)
Distance
H-bond
Metal coordination
Pi-Pi stacking
Pi-cation
Salt bridge
Solvent exposure

Figure 3

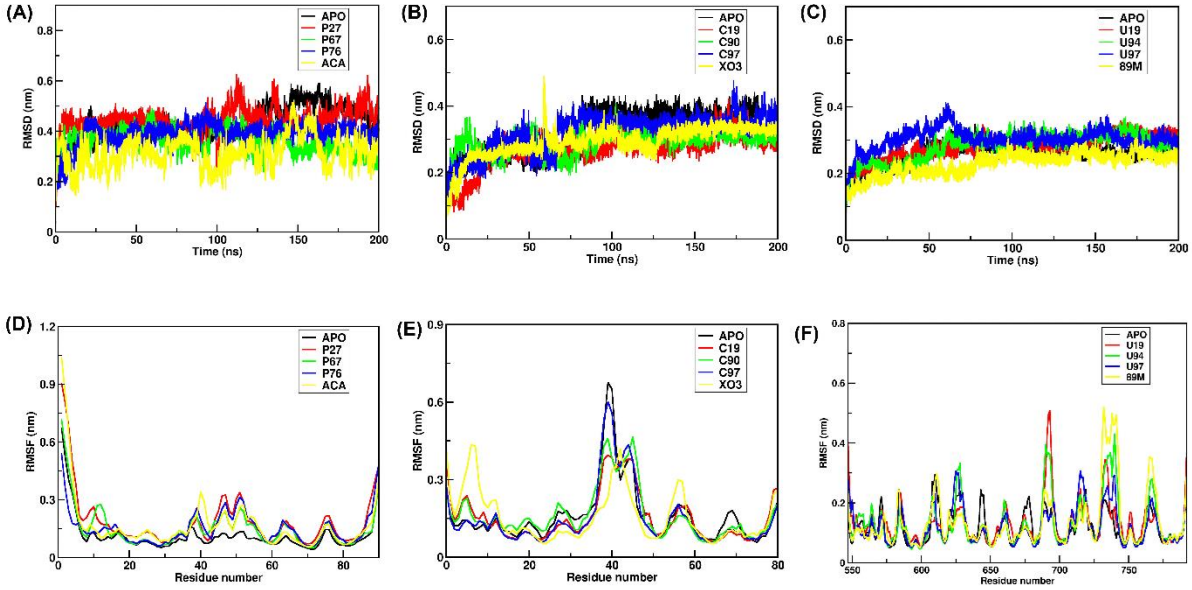

Figure 4

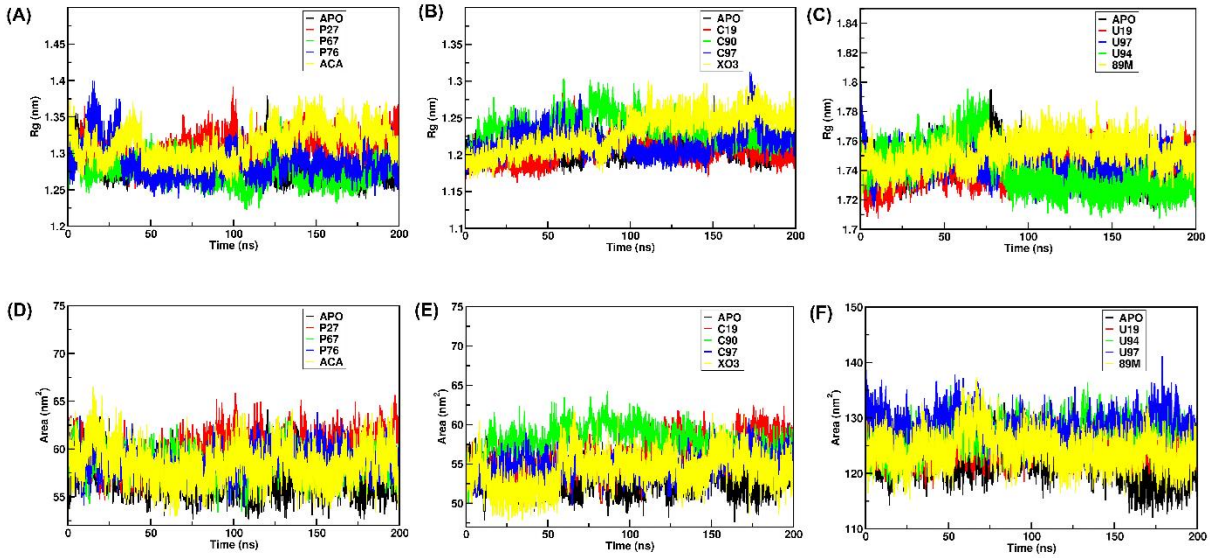

Figure 5

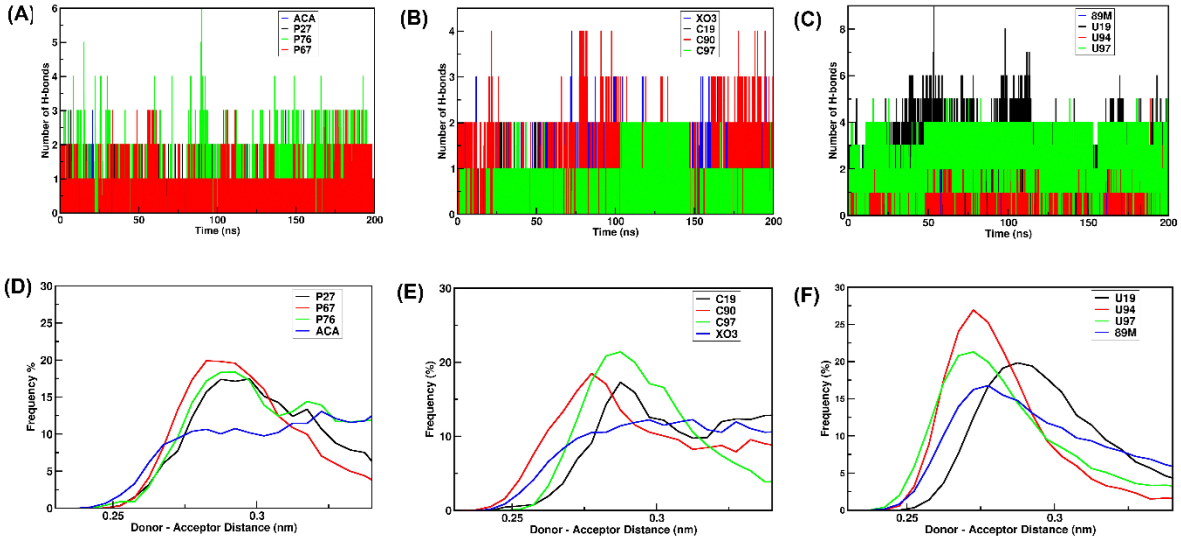

Figure 6

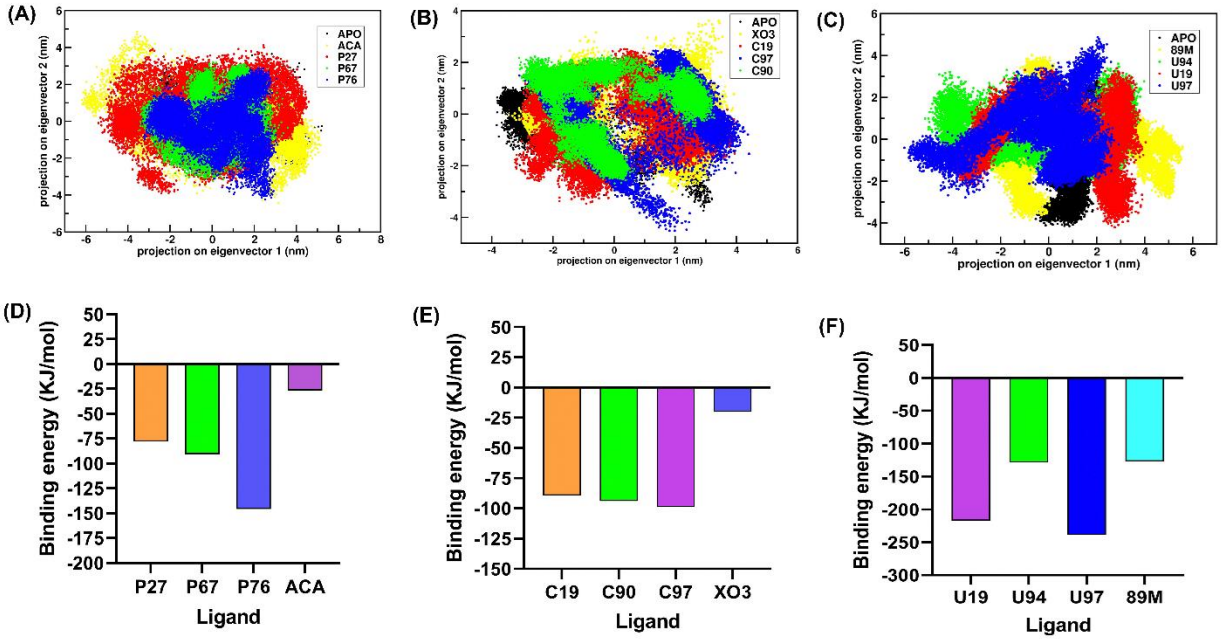

Figure 7

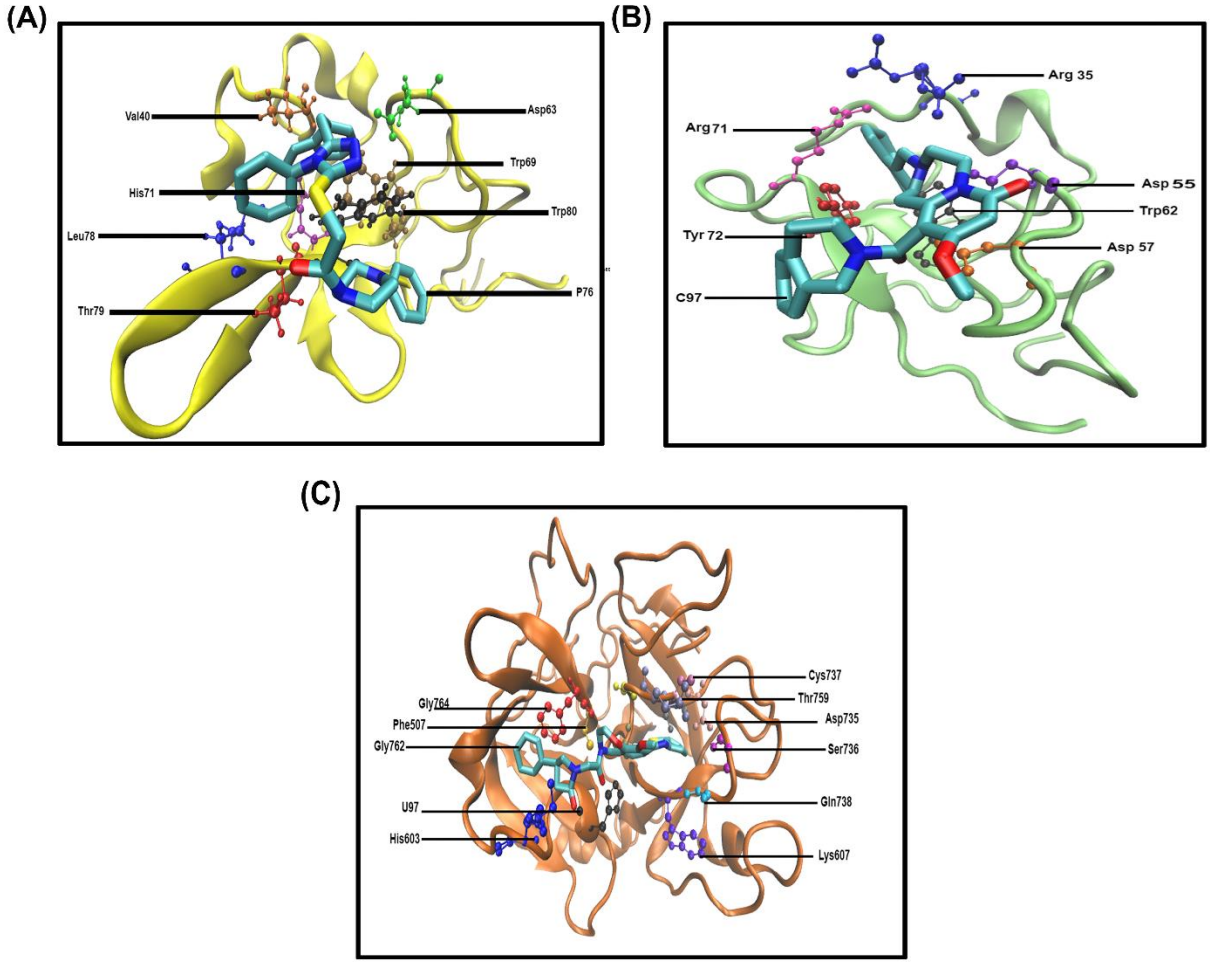
(A)
Val40
Asp63
Trp69
His71
Trp80
Leu78
P76
Thr79
(B)
Arg 35
Arg71
Asp 55
Trp62
Tyr 72
Asp 57
C97
(C)
Cys737
Thr759
Gly764
Asp735
Phe507
Ser736
Gly762
Gln738
U97
His603
Lys607

Figure 8

Table 1: Molecular docking results of top nine identified ligands (P27, P67, P76, C19, C90, C97 U19, U94, U97) and the reference ligands (ACA, XO3, and 89M) bound with their respective protein targets (1PK2, 4CIKand 5UGG) using three docking tools: Autodock vina, ParDOCK/BAPPL+, and Glide respectively.

Protein target	Ligands	Autodock Vina-Binding Energy (Kcal/mol)	ParDOCK and BappL-Binding energy (Kcal/mol)	Glide Score	Interacting residues
1PK2	P27	-8.3	-9.6	-9.31	LYS39, VAL40, TYR41, ASP63, TRP69, HIS71, ARG77, LEU78, THR79, TRP80, GLU81, TYR82
	P67	-7.6	-8.84	-8.6	GLU23, LYS39, VAL40, TYR41, HIS71, ASP63, TRP69, ARG77, LEU78, TRP80, GLU81, TYR82
	P76	-8.9	-9.63	-9.42	LYS39, VAL40, TYR41, TRP69, HIS71, ARG77, LEU78, THR79, TRP80, GLU81, TYR82
	ACA	-3.9	-4.9	-7.25	LYS39, VAL40, TYR41, ASP63, ASP65, LEU78, THR79, TRP80, TRP69
4CIK	C19	-8.5	-9	-8.92	ARG35, ASP55, ASP57, PRO58, GLN59, TRP62, TYR64, ARG71, TYR72, TYR74
	C90	-8.2	-8.9	-8.75	ARG35,ASP55, ASP57, GLN59, TRP62, GLU69, LYS70, ARG71,TYR72, ASP73, TYR74
	C97	-8.8	-9.47	-9.3	ARG35, PHE36, ASP55, ASP57, PRO58, GLN59, TRP62, TYR64, ARG71, TYR72, TYR74
	XO3	-7.4	-6.66	-7.15	ARG35, PHE36, ARG71, TYR72, TYR74, TYR64, TRP62, ASP55, ASP57
5UGG	U19	-10.9	-7.9	-8.87	HID63, CYS64, LEU65, GLU66, LYS67, SER68,

					ARG70, SER72, SER73, TYR74, GLN198, SER201
	U94	-11	-8.02	-9.41	SER68, LYS67, TYR74, GLU66, LEU65, CYS64, HID63, CYS197, SER196, ASP195, VAL233, GLY232, CYS225, GLY224, LEU223, GLY222, TRP221, SER220, SER201
	U97	-11.4	-8.33	-9.6	ALA62, HID63, CYS64, LEU65, GLU66, LYS67, SER68, TYR74, SER73, CYS197, SER196, ASP195, GLY232, VAL233, SER220, TRP221, GLY222, LEU223, GLY224, SER201
	89M	-9	-5.9	-7.5	SER68, LYS67, GLU66, LEU65, TYR74, PHE47, CYS64, HID63, GLY146, GLU147, THR148, GLN198, GLY199, SER201, SER220, TRP221, GLY222, LEU223, GLY224

Table 2: MMPBSA detailed energies (Binding energy and the individual energy components van der Waal energy (ΔE_{vdW}), electrostatic energy (ΔE_{elec}), polar solvation energy ($\Delta G_{polar\text{-}solv}$), SASA energy ($\Delta G_{non\text{-}polar}$) of all the protein-ligand complexes.

	MMPBSA DETAILED ENERGIES					
Protein target	Ligands	van der Waal energy	Electrostatic energy	Polar solvation energy	SASA energy	Binding energy
1PK2	P27	-118.529 +/- 17.130 kJ/mol	-5.881 +/- 6.590 kJ/mol	61.449 +/- 21.931 kJ/mol	-15.014 +/- 1.943 kJ/mol	-77.975 +/- 19.181 kJ/mol
	P67	-117.567 +/- 47.692 kJ/mol	-12.887 +/- 9.387 kJ/mol	51.918 +/- 28.232 kJ/mol	-12.262 +/- 5.059 kJ/mol	-90.798 +/- 37.674 kJ/mol
	P76	-171.612 +/- 24.161 kJ/mol	-0.102 +/- 3.913 kJ/mol	42.307 +/- 10.310 kJ/mol	-16.246 +/- 2.225 kJ/mol	-145.653 +/- 20.078 kJ/mol

	ACA	-40.822 +/- 9.960 kJ/mol	-5.951 +/- 6.304 kJ/mol	27.127 +/- 13.044 kJ/mol	-6.815 +/- 1.117 kJ/mol	-26.460 +/- 9.222 kJ/mol
4CIK	C19	-178.135 +/- 49.112 kJ/mol	-19.139 +/- 11.123 kJ/mol	126.667 +/- 27.807 kJ/mol	-18.703 +/- 4.933 kJ/mol	-89.31 +/- 39.414 kJ/mol
	C90	-178.135 +/- 49.112 kJ/mol	-8.939 +/- 11.123 kJ/mol	111.896 +/- 27.807 kJ/mol	-18.703 +/- 4.933 kJ/mol	-93.881 +/- 39.414 kJ/mol
	C97	-128.666 +/- 35.350 kJ/mol	0.790 +/- 3.810 kJ/mol	41.817 +/- 25.156 kJ/mol	-12.890 +/- 3.743 kJ/mol	-98.949 +/- 32.293 kJ/mol
	XO3	-45.470 +/- 7.831 kJ/mol	-6.123 +/- 7.523 kJ/mol	38.916 +/- 27.368 kJ/mol	-7.388 +/- 1.775 kJ/mol	-20.066 +/- 30.373 kJ/mol
5UGG	U19	-326.449 +/- 12.469 kJ/mol	-28.751 +/- 14.338 kJ/mol	164.799 +/- 11.051 kJ/mol	-26.749 +/- 0.969 kJ/mol	-217.150 +/- 16.376 kJ/mol
	U94	-193.346 +/- 18.772 kJ/mol	-24.924 +/- 13.795 kJ/mol	106.994 +/- 23.339 kJ/mol	-17.398 +/- 1.411 kJ/mol	-128.674 +/- 20.963 kJ/mol
	U97	-332.423 +/- 12.146 kJ/mol	-28.614 +/- 7.827 kJ/mol	148.128 +/- 10.778 kJ/mol	-25.937 +/- 1.160 kJ/mol	-238.846 +/- 17.788 kJ/mol
	89M	-199.690 +/- 9.099 kJ/mol	-30.462 +/- 10.217 kJ/mol	126.314 +/- 23.798 kJ/mol	-23.143 +/- 1.662 kJ/mol	-126.981 +/- 19.836 kJ/mol

24